DEVELOPMENT OF AN INTERACTIVE IMAGE-GUIDED NEUROSURGICAL SYSTEM

Thesis submitted for Masters of Science in Biomedical Engineering

Department of Human Biology
University of Cape Town
March 2004

Student: Megan J. Watson
Supervisor: Dr. Ernesta Meintjes

DEVELOPMENT OF AN INTERACTIVE IMAGE-GUIDED NEUROSURGICAL SYSTEM

Student: Megan Watson
Supervisor: Ernesta Meintjes

Submitted to the University of Cape Town in partial fulfilment of the requirements for the degree of Masters of Science in Medicine, in Biomedical Engineering

March 2004

ACKNOWLEDGEMENTS

First I would like to thank my supervisor Ernesta Meintjes for her support and guidance.

I would like to thank Andre Bester for his help and contribution to the project.

Thank you to the Neurosurgeons Allan Taylor, Graham Fieggen and Jonathon Peter for their contributions.

Thank you to Christopher Vaughan, Harry Hall, Electronic Development House and Fernando Martinez for their contribution in the development of this project.

Thank you to my family and friends for their support and encouragement.

ABSTRACT

The aim of this project is to develop an interactive image-guided neurosurgical system. Three technologies for three-dimensional (3D) measurement were investigated and the method of choice developed.

The Prototype Navigator was based on the principle of Peppers Ghost and utilized a Reflex Metrograph to perform 3D measurements. The system consisted of a probe, the Metrograph and a transparent mirror positioned mid way between. Two methods were employed to investigate the accuracy and repeatability of the system. The first used a pumpkin and followed the standard surgical procedure. The accuracy was determined to be $2.4 \pm 0.5mm$. The second used a phantom consisting of 15 points, whose coordinates are accurately known, arranged in a 3D volume. The accuracy was determined to be $2.4 \pm 0.7mm$. The repeatability is $1.3 \pm 0.5mm$ with a maximum error, between repeated measurements of the same point, of $2.0mm$. The accuracy is very good and is comparable with the measured accuracy of commercial systems. The Prototype Navigator has been successfully used in several operations. However, the system has several notable limitations such as the need for an experienced user to achieve good accuracy. For this reason the Metrograph in the Prototype Navigator has been replaced.

Zebris, an ultrasound 3D EEG positioning system, was investigated as a possible replacement of the Metrograph. The system consists of a receiver, a pointer and three reference transmitters positioned around the face to correct for movement. The system accuracy, repeatability and effect of movement on the repeatability were investigated using the 15-point phantom. The accuracy was determined to be $2.4 \pm 1.0mm$ with a maximum error of $4.5mm$. The repeatability was determined to be $4.3 \pm 1.7mm$ with a maximum error of $8.4mm$. Although the accuracy is good, very low repeatability makes the system unsuitable for application in neurosurgery.

The stereo-photogrammetric system consists of the following components: the probe, control frame, enclosure containing the smart cameras, stand, software, and laptop. The stand with the enclosure mounted on it is clamped to railings that run along either side of the surgical table. The laptop and the cameras execute software that communicates via an Ethernet link.

The laptop triggers the cameras to take a stereo pair of images. The software on each camera applies a pattern recognition algorithm to each of the images to extract the 2D coordinates of the markers that appear on the control frame or probe. The 2D coordinates of the pair of images are downloaded to the laptop where a direct linear transformation is applied to find the 3D coordinates. The coordinates are transformed into CT space using fiducials of which both the CT and theatre coordinates are known, and the position of the tip of the probe is displayed on the nearest CT slice.

The system was tested under laboratory and theatre conditions. Two methods were employed to investigate the accuracy in the laboratory. The first method followed the surgical procedure where the CT coordinates of the measured points were compared to the coordinates obtained from the CT scans. The accuracy was determined to be $2.0 \pm 1.1mm$ using the head phantom and $2.6 \pm 1.1mm$ using the rod phantom. The second method followed the same procedure except the physical space coordinates of the measured points were transformed into the calibrated reference frame and compared to the more accurate calibrated coordinates. The accuracy was determined to be $2.0 \pm 0.8mm$. The theatre investigation used the first method and determined the accuracy to be $1.6 \pm 0.8mm$.

The repeatability was determined to be $1.9 \pm 1.1mm$ with a maximum error of $4.7mm$ in the laboratory and $3.8 \pm 1.4mm$ with a maximum error of $6.0mm$ in theatre. The calibration and recognition accuracy were investigated and found to be very good. The effect of the operating lights on the calibration in theatre was determined to be insignificant.

The accuracy of the system is comparable with systems in commercial use and has been approved by the neurosurgeons involved for use in clinical trials. Currently the system requires the set up to be performed by someone familiar with the system but once in operation it is simple and easy to use. It will be modified to use off-the-shelf digital cameras or to function as a stand-alone system and developed into a commercially viable product.

TABLE OF CONTENTS

LIST OF FIGURES

LIST OF TABLES

CHAPTER 1

Introduction

The removal of a lesion or tumour from the brain is a complex task requiring an intricate knowledge of the anatomy of the brain. The precise awareness of the complex three-dimensional anatomic relationships is vital for the successful removal of the lesion. This skill is acquired through many hours of study and clinical experience, and forms a major part of the neurosurgeons training. This navigational skill is challenged by distortion of the anatomic relationships through the pathology of disease, by limited fields of view and oblique approaches as well as anatomic variations between patients. Essentially the neurosurgeon requires a map of the brain displaying the precise location of the lesion for surgical navigation.

Image-guidance provides a means of surgically navigating through the brain and removing a lesion with minimum damage to the surrounding healthy tissue. To achieve this it is essential to locate accurately in three-dimensions the position of the tip of a surgical instrument relative to the position of the lesion as determined pre-operatively using an imaging modality such as computed tomography (CT).

The images obtained using CT or some other imaging modality define a volume within the coordinate system of the scanner. A frame of reference is defined within this volume by positioning fiducial markers around the patient's head as points of reference. The fiducials occupy specific positions in both the CT coordinate system and physical space and are used to map the images onto physical space. In this manner the images are registered to physical space. This registration provides a map for precise three-dimensional (3D) surgical navigation.

Maciunas RJ (1993) described an ideal Interactive Image-Guided Neurosurgical System as universal, intuitive and robust. The ideal system would have the following

functionality: The ability to register medical images to one another and to physical or theatre space for surgical localisation. Registered images would be employed to plan the surgical approach pre-operatively. An intra-operative localisation device or pointer would be used to trigger a real-time display of the surgical position. High localisation accuracy and precision are essential. The system would include the ability to integrate alternative intra-operative localisation methods and to compare pre-, peri- and post-operative scans.

At the time of writing such a system did not exist although several commercial systems now achieve these objectives. Brainlab's VectorVision² (Brainlab AG, Heimstetten, Germany) and Medtronic's StealthStation® Treon™ (Medtronic Surgical Navigation Technologies, Louisville, Colorado) are two such examples.

Various technologies have been used for the 3D location of a surgical instrument. These are outlined in the literature review section that follows. Unfortunately, commercial systems that track the position of a pointer in the brain are unaffordable to government-funded hospitals in developing countries.

For this reason a prototype system had been developed through a close collaboration between the MRC/UCT Medical Imaging Unit and the Department of Neurosurgery at the University of Cape Town. The prototype navigation system, based on the principle of Pepper's Ghost, used a Reflex Metrograph (Scott PJ, 1981) to perform 3D measurements in theatre. However, this system, shown in figure 1.1, has several disadvantages: the equipment is large and bulky and requires a trained person to be present to operate the Metrograph.

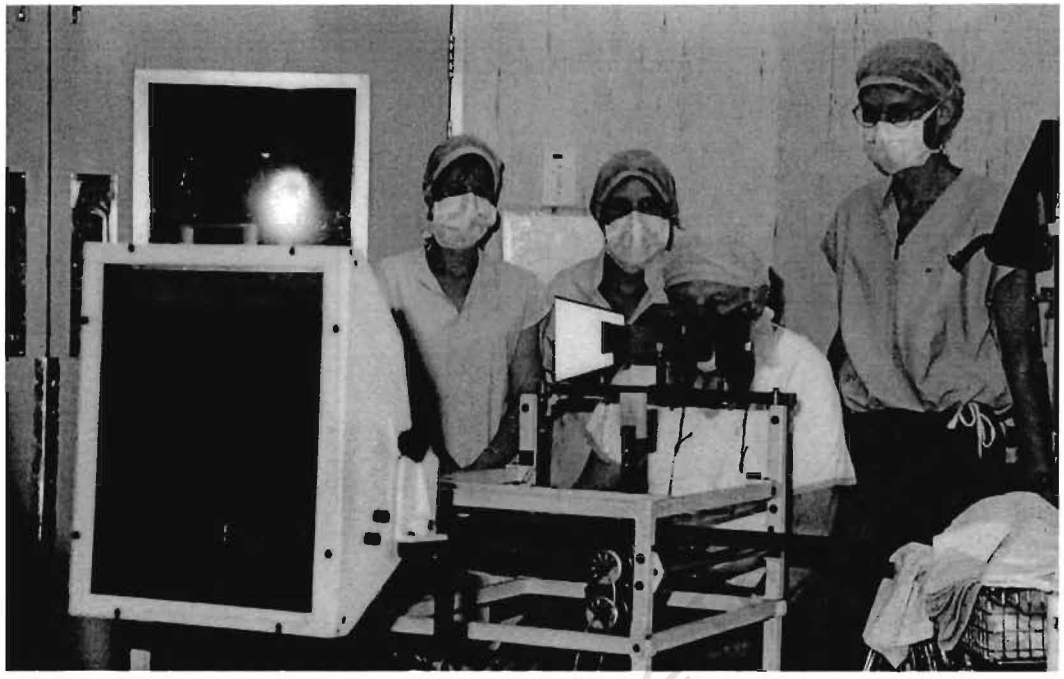

Figure 1.1: The Metrograph and mirror in theatre

This thesis explores the feasibility of various proposed alternative technologies to measure the 3D position of a surgical instrument in theatre and describes the development of the technology of choice for such an interactive image-guided neurosurgical system.

Chapter 2 describes the pattern recognition algorithms and photogrammetric theory employed by the system. Photogrammetric theory covers the principle behind the reconstruction of 3D object data using two-dimensional (2D) image data extracted using the pattern recognition algorithms. Camera calibration and the principle of perspective projection are outlined. Finally the algorithms used to reconstruct the 3D data are described.

The next few chapters describe the investigation of three alternative technologies for the 3D measuring device.

Chapter 3 investigates the accuracies achievable with the Prototype Navigation System (Metrograph). Chapter 4 investigates the feasibility of using an ultrasound-based EEG positioning system, specifically Zebris (Zebris Medizintechnik GmbH, Isny—Tübingen, Germany) (http://www.zebris.de/), as the 3D measuring device.

Chapters 5 and 6 describe the third 3D measuring device and method of choice investigated for surgical guidance, namely stereo-photogrammetry. The components of the stereo-photogrammetric system are explained and their design issues described in chapter 5. Chapter 6 describes the software developed for the system. This is divided into two areas: The software running on the laptop and the software running on the smart cameras. The communication between the laptop and the smart cameras is also described.

Chapter 7 describes the testing process for the stereo-photogrammetric system in the laboratory as well as initial theatre tests using a phantom head.

In chapter 8 the conclusions of the project are presented.

1.1 Literature Review

This section explores the history of and some of the technological advances for measuring objects in 3D space. It then introduces photogrammetry and its application to neurosurgery.

Neurosurgical navigation has many useful applications, the most common of which is probably the resection of subcortical and deep tumours (McInerney J and Roberts DW, 2000). Navigation can be used to determine the precise location of a tumour and plot a trajectory of approach prior to the craniotomy. It has application in vascular malformations, epilepsy, endoscopy and the spine. Wuttipong T, et al. (2003) used it for

accurate planning of the craniotomy, identification of the distal sylvian fissure, and finding the site for insular corticotomy.

The first systems for guiding a surgical instrument to a specified point within the brain were stereotactic frames fixed to the patient's head. The frame both defined a coordinate system, which could be related to the images of the patient's head and provided a guide for the biopsy needle or an electrode. The concept of stereotaxy came about in 1906 (Kelly PJ, 2000). Robert H Clarke and V. Horsley developed this concept and the first stereotactic frame was patented in 1912. However, stereotaxy wasn't used on human patients until EA Spiegel and HC Wycis at Temple University, Philadelphia, performed the first clinical trial in 1947. Initially stereotactic methods were applied to the study of movement disorders where point-based single trajectory methods are used. In the late 1970s and early 1980's with the advent of CT and later magnetic resonance imaging (MRI) scanning, image-guidance was incorporated into stereotactic methods. Stereotactic systems are, however, non-intuitive for the surgeons, are cumbersome to use, and cause the patient discomfort.

In Dartmouth in 1981 a project was undertaken to replace the stereotactic frame with a non-contact 3D measuring device. The first frameless stereotactic prototype employed an operating microscope and sonic technology (Roberts, 1986).

Three microphones mounted on a rigid support to define the coordinate system of the operating room and three sonic emitters attached to the microscope (figure 1.2) with a fixed relationship to the focal plane for tracking of the focal plane. Registration was achieved using 3 fiducials attached to the scalp during CT scanning. The focal plane of the microscope is used as a pointer and focused on each fiducial in turn defining the transformation between CT and theatre space.

During the operation the microscope is freely positioned, if CT data is desired the acoustic localiser is activated and a CT derived contour superimposed on the operating field. The mean accuracy was found to be less than 2mm. The accuracy of the focal

point localiser was found to be between 1 and 3mm. The system was employed in a clinical setting in 1984 (Roberts, 1992).

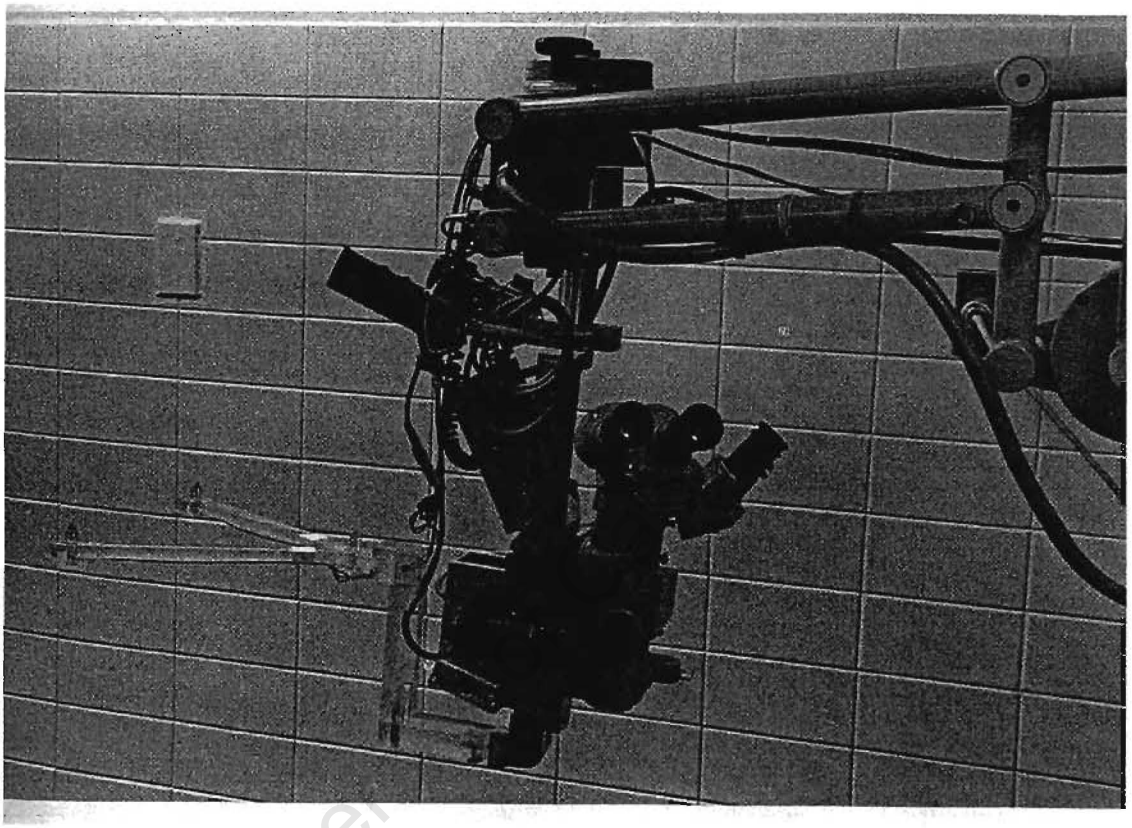

Figure 1.2 The Sonic Digitising Microscope (Roberts, 1992)

The original method of patient registration (Barnett, et al, 1998) used fiducial markers to register CT images to physical space. A number of alternatives now exist. Anatomical landmarks can replace the markers used as fiducials in the previous example. The algorithms used in registration are the same for the two methods. Facial landmarks, however, result in lower accuracies because of the less discrete nature of the features. A different method using non-ordered points is surface matching. A set of randomly chosen data points on the face are measured and used to define a surface contour of the face. This surface is compared to one constructed from the CT or other imaging

modality images, usually employing an iterative optimisation algorithm. While this technique is easily automated, it has the disadvantage that it can appear to achieve optimisation when it has not. The method is slower and less accurate than point-based marker registration but does not require an additional scanning session nor does it require adhesive markers to be attached to the patients scalp. With current advances in technology surface matching algorithms are becoming faster and more accurate. The z-touch by Brainlab (figure 1.3) and the Fazer Contour laser by Medtronic are quoted as being fast and accurate.

Figure 1.3 The z-touch from Brainlab (Brainlab AG, Heimstetten, Germany)

Raabe A, et al. (2002) performed a study employing the z-touch for patient registration and VectorVision² (Brainlab) for surgical navigation. The study concluded that laser scanning is accurate, robust and easy to use. The nasion, forehead, and medial, superior and lateral rim of the orbita are typically scanned since the bony contours are easily distinguishable. The disadvantage of the area is that the system accuracy decreases towards the occipital lobe. The system accuracy is $1.8 \pm 0.8mm$ for lesions near the front and $2.8 \pm 2.1mm$ for lesions further back. The overall accuracy is $2.4 \pm 1.7mm$.

Germano IM, et al. (1999) performed a comparison of the three methods using the StealthStation® (Stealth Technologies, Boulder, Colorado). The surface-based algorithm used the transformation parameters obtained using the facial landmarks as a starting point for the optimisation routine. The point-based algorithm using markers was found to be the most accurate with an error of $1.7 \pm 0.2mm$, the same algorithm using facial features as fiducials was found to be $3.4 \pm 0.2mm$. The surface-based algorithm improved on this error and was found to be $2.3 \pm 0.3mm$, which is similar to the accuracies achieved by the z-touch system.

A study performed by Suess O, et al. (2001) using the NEN-NeuroGuard™ neuronavigation system (Nicolet Biomedical, Madison, WI, USA), an electromagnetic navigation system, found a mean registration error of $1.3mm$ with MRI-data and $1.5mm$ with CT-data. Seven adhesive skin fiducial markers were employed in the registration. The accuracy is comparable with that determined by Germano, et al. (1999) using point-based registration. The difference between point-based and surface-based registration accuracy is small and with further technological advances surface-based registration will become faster and more accurate. Currently however, point-based registration is a faster, more reliable and cheaper method.

The system accuracy of the NEN-NeuroGuard™ was found to be $0.8mm$ (with a range of $0.3mm$ to $1.5mm$) using a plastic phantom and $3.2 \pm 1.5mm$ after dural opening during surgery. The decrease in accuracy is due to skin movement and brain shift. After removal of part of the tumour the error increased to up to $24mm$. The use of intra-operative ultrasound can reduce the effect of brain shift. Bonsanto, et al. (2001) found intra-operative ultrasound easy to use as well as being cheaper and less cumbersome than intra-operative MRI or CT. The study described the initial experiences with the UltraWand® (MISON, Trondheim, Norway). Intra-operative ultrasound started gaining acceptance in the 1970's with the availability of the high-frequency B-mode. However, the low image quality prevented it gaining wide spread acceptance. Now with advances in image quality and the use of 3D reconstruction in the UltraWand® it is proving itself a contender with conventional Stereotactic methods.

Presented below is a summary of the most widely used technologies that have been employed in 3D measuring systems (Barnett GH, 1998).

1.1.1 Sonic

Ultrasound systems are the earliest technology employed in image-guided neurosurgery techniques and date back as far as 1984. The systems use emitters fixed on a probe, which produce an ultrasonic pulse that is detected by an array of microphones fixed in a known configuration. The distance between the microphone and emitter is calculated from the time delay between the production of the pulse and its detection using the speed of sound.

Sonic technology is inexpensive, simple and the systems are robust. They need no alignment, have a large working volume and are quick to set-up. The systems are also accurate at localization.

The disadvantages are that line-of-sound is required between the detector and emitters and that they must be in close proximity to achieve the required accuracy. The system is susceptible to environmental noise and drafts, and ultrasonic noise from the suction pumps.

The first prototype Neurosurgical Guidance System employing sonic technology was the Sonic Digitising Microscope described previously.

A system currently in use that employs sonic technology for 3D measurement is the Zebris System (see chapter 4), an EEG electrode positioning system.

1.1.2 Jointed Robotic Arms

Jointed robotic arms were used in the first frameless stereotactic systems developed alongside the Sonic Digitising Microscope. One of the first prototypes of such a system is The Neuronavigator (Watanabe E, et al, 1987), shown in figure 1.4. This system uses a potentiometer based jointed arm and accuracies of 1.33mm (Watanabe, 1993) have been reported.

The base of the arm is typically fixed to the head immobiliser allowing the system to track any head movement. The arm consists of several segments of known length. The joints linking the segments contain sensors to determine the angles. Using the angles and known lengths, the location and orientation of the tip can be calculated.

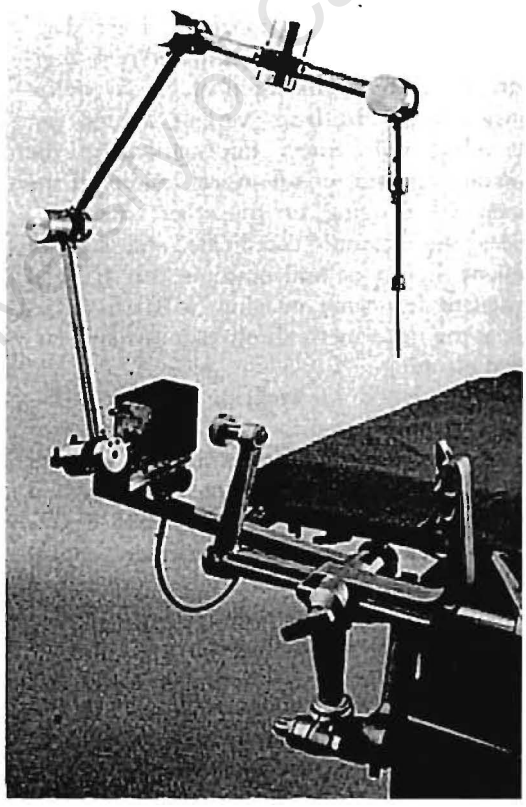

Figure 1.4 An example of a jointed arm system: the Neuronavigator

One advantage of this system is that it allows for tracking of head movement since the arm is fixed to the head immobiliser. In addition the system is simple and is an established technology. There are no line-of-sight requirements.

However, it may not always be possible to position the tip in a desired spot, it is awkward to use, bulky, and is conceptually foreign to the surgeon. Either electrical sensors, which are cheap but subject to drift, or digital sensors, which are accurate but expensive, may be used.

Another example is the ISG Viewing Wand. The Wand consists of a six-jointed arm with electrogoniometers on the joints. The system accuracy has been determined to be $1.67 \pm 0.43mm$ with a variance of $0.2mm$ (Benardete EA, et al, 2001).

1.1.3 Magnetic

Magnetic systems apply a magnetic field over the surgical workspace. The probe is able to detect gradients in the magnetic field, which are used to determine the 3D position of the tip of the probe.

The main advantage is that no line-of-sight is required and there is no mechanical link to the system. Metal objects placed within the field may however, result in spurious localization. This effect is minimized by the use of alternating current.

A commercially available system using a magnetic field is the Cygnus PFS System. The mean error of the Cygnus PFS has been reported as $1.9 \pm 0.7mm$ with a variance of $0.34mm$ (Benardete EA, et al, 2001).

Another system employing electromagnetic technology is the Magellan Frameless Stereotactic System. The Magellan employs a passive, mini, electromagnetic position sensor encapsulated in a flexible or shapable probe. A location pad positioned close to

the surgical field generates the electromagnetic field. The position of the sensor is located relative to a reference probe attached to the skin of the patient. A study performed on the system determined the mean error to be $1.03mm$, although this appears to vary with the distance between the location pad and cranial base (Zaaroor M, et al, 2001). The system has the ability to track probes within the brain and was not noticeably affected by the introduction of surgical instruments in the electromagnetic field.

1.1.4 Optical

Optical systems use a camera array to detect light from either active emitters or passive reflectors.

The active emitters, usually light-emitting diodes (LED's) are pulsed sequentially to conserve their life as well as to differentiate the emitter from background light and the other emitter(s) attached to the probe. The light used is typically near infrared and therefore invisible to the human eye. The light is detected by solid-state cameras composed of either linear or 2D charge coupled devices (CCD's). The intense operating lights can cause reflections, which may lead to confusion and inaccuracies. The limitation of this system is that line-of-sight is required. It is, however, silent and repeatable.

Passive reflectors work in the same manner as active emitters except that the light has a different source and is reflected off them. The advantage of these is that they are wireless and autoclavable. If there are too many reflectors confusion and inaccuracies may result from difficulties in distinguishing between them.

Optical systems may use either linear or 2D CCD cameras. Linear CCD's consist of tens of thousands of elements in a linear arrangement. Light is focused on the elements and the strongest illuminated is used for localization. Three or more of these sensors

are required to acquire 3D coordinates. The advantage to using linear CCD's is that they have a high resolution. In addition, the main part of the processing occurs in a "black box" and not in the software, therefore producing the 3D coordinates faster than with 2D CCD's. The disadvantages are that they require precise, stable alignment to be repeatable and are expensive. The Optotrak (figure 1.5) from Northern Digital Inc. (Waterloo, Canada) (http://www.ndigital.com/) is an example of a system using three linear CCD detectors. The root mean square (RMS) accuracy has been quoted as $0.1mm$ in the x and y direction, and $0.15mm$ in the z direction.

Figure 1.5 The Optotrak 3D measuring system from Northern Digital

Conventional 2D CCD's consist of elements arranged in a rectangular configuration. Such systems employ photogrammetric techniques to acquire a set of images and then apply a direct linear transformation (Abdel-Aziz YI and Karara HM, 1971) or some other algorithm to compute the 3D coordinates of a point. The advantages of using 2D CCD's are that they are precise and, if low-resolution CCD's are used, they are cheaper than linear ones. However, they also require precise, stable alignment. Image processing is performed by software making such systems slower than ones using linear CCD's.

Machine Vision (Barnett GH, 1998) is an entirely passive system. It consists of two or more video cameras in a known geometric configuration aimed at the surgical field. Surgical tools within this field are compared to a reference set of surgical tools of known geometries; passive markers may be used to assist recognition, however, special

illumination, for example ultra-violet, is not required. As with all optical systems it requires line-of-sight.

A machine vision system implemented by Heilbrun MP (1993) is shown in figure 1.6. This system employs two cameras placed 1m apart and roughly 2m above the surgical workspace. The coordinate system of the surgical workspace is calibrated using a video localiser consisting of 8 fiducial objects of known dimension in a cubic configuration. The 2D coordinates of these objects are measured from a pair of digitised images. A photogrammetric projection algorithm (to be described in chapter 2) is used to compute the 3D coordinates. The 3D coordinates of any point can now be established.

The spatial relationship between the object in the surgical workspace and the imaging modality, in this case CT, is computed using a transformation matrix to accomplish the rotation, translation and scaling of points moving between coordinate systems (see chapter 2). A minimum of 3 points located in both systems is required to achieve this objective.

Figure 1.6 The machine vision system by Heilbrun, demonstrated using a phantom head

A commercially available optical system, the SMN Pointer, employs infrared LED's and linear CCD's. The mean error has been reported to be $2.26 \pm 0.83mm$ with a variance of $0.36mm$ (Benardete EA, et al, 2001).

1.1.5 A Brief Overview of Photogrammetry

Photogrammetry is defined as the science of making reliable measurements from the use of photographs. It covers a broad field of use, amongst which aerial, terrestrial, satellite, analytical and stereo-photogrammetry. Image-guided neurosurgery is an application of close-range stereo-photogrammetry.

Close-range photogrammetry is defined as having a maximum distance, between the cameras and the object being imaged, of 300m and a minimum distance of a fraction of a millimetre (Karara HM, 1989). Close-range photogrammetry is used in medical applications. Medical photogrammetry was first discovered in 1863 when Holmes used stereo photographs to study human gait (Fryer JG, 1996). Today it has a broad range of applications including surgery, anthropomorphic measurements, gait analysis and patient monitoring. Potential advantages for medical applications are:

- It is non-invasive
- There is no distortion of object surface due to contact
- It allows measurement of non-rigid and moving objects
- The photographic and measurement phases are separate
- Provides a permanent 3D record that can be easily stored and re-measured at any time
- Versatile, can measure both simple and complex objects
- Data obtained are suitable for manipulation by computer
- The data acquisition is rapid therefore the digital images are available immediately

- Analytical methods provide a means to integrate the image acquisition with the calculations performed on the images
- The invisible part of the spectrum can be used for creating images
- Off-the-shelf equipment may be used, decreasing the overall cost

1.1.5.1 Image-Guided Neurosurgical Systems

The photogrammetric system developed as part of this thesis is a stereo-photogrammetric interactive image-guided neurosurgical system (SIIGNS). Photogrammetric methods are used to locate a probe or pointer in space. The probe contains three markers arranged in a triangular configuration, which are used to locate its tip. Three markers in a triangular configuration yield increased accuracy of localisation of the tip compared to the conventional two markers in a linear configuration with the tip. The Rodrigues Matrix (described in Chapter 2), which is used to compute the coordinates of the tip of the probe, requires at least 3 points of which the coordinates are known. In theatre space the probe is positioned with the tip in the area of interest. A CT or MRI scan or other diagnostic image is displayed showing the position of the tip of the probe with respect to the lesion or point of entry.

The system was designed as an affordable alternative for government-funded hospitals in developing countries. The final cost of the system is estimated at R400 000 to R500 000. This cost can be greatly reduced by utilising off-the-shelf digital cameras as opposed to the smart cameras used currently. Comparatively the cost of commercial systems ranges from US$100 000 (approximately R700 000*) to R2.5 million. Pure 3D measurement systems, such as the Optotrak from Northern Digital Inc. (Waterloo, Canada), range in price from US$ 24 000 (approximately R168 000*) to US$63 000 (approximately R441 000*). These systems while quoted at a lower cost are purely for

* Exchange rate of 1US$ to R7

3D measurement and would require additional software development for use in image-guided neurosurgery applications, consequently increasing the overall cost.

The system differs from commercially available neurosurgical systems in two key areas. The first is the use of smart camera technology. The smart cameras contain a StrongARM 206 MHz processor (2d3D Inc, South Africa) running a version of Linux adapted for the processor board. This enables an application to be developed and run on the cameras. This has several advantages:

- All the processing is done on each of the cameras making the system faster and requiring less memory space on the connected computer.
- It can be used in real time
- No need to download photos, only results or coordinates, which makes processing time faster
- Can be used over a network

Secondly, the control frame used (refer to Chapter 5) for calibration of the operating space differs from those used in commercial systems. Accurate calibration allows for accurate measurements during the operation. The frame is made up of $6mm$ bars enclosing a volume of $250 \times 200 \times 150mm$. There are twelve markers attached to the frame, spaced to cover the entire volume enclosed by it. The markers are passive infra-red reflective circles. The frame is used before the start of each operation. It is held in position above the patient's head while the cameras are triggered. The frame is briefly held in position rather than mounted for the duration of the operation, since its position directly above the surgical space would obstruct the surgeon. In clamping the frame to the surgical table the possible risk of injury to the patient is increased also.

By comparison one of the commercially available systems, Brainlab IGS VectorVision² Cranial (Figure 1.7), uses a reference frame, shown in figure 1.8, consisting of 3 passive reflective markers fixed near the surgical area. The reference frame or Mayfield adaptor attaches to the Mayfield clamp. It is used to achieve real time imaging of the

patient's head movement during surgery. It allows the patient to be re-registered without needing to measure the burr points as long as the frame remains fixed relative to the patient's head. However, only the space enclosed by the markers on the reference frame is calibrated and the coordinates obtained within the surgical area are being extrapolated.

Calibration is achieved by moving a calibration rod in front of the cameras prior to the operation. Infrared light emitting diodes (LED's) are positioned around the cameras.

Figure 1.7 Brainlab VectorVision²

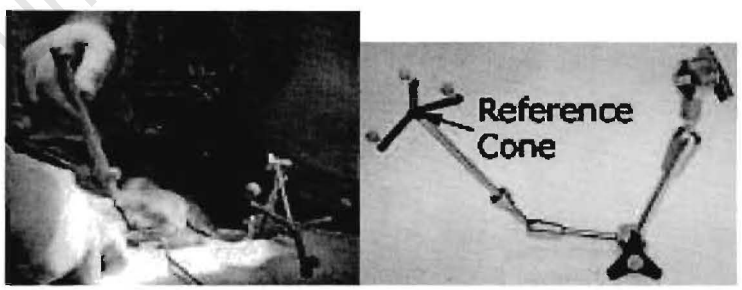

(a) *(b)*

Figure 1.8 (a) The Brainlab reference frame array depicted during a spinal procedure, the pointer is also displayed. (b) The reference frame is shown clamped to the Mayfield adaptor, which attaches to the Mayfield clamp during surgery. The reference frame contains a calibration cone at the juncture of the three arms for calibrating the tip of a surgical instrument attached to an instrument adaptor.

The Brainlab system utilises an "instrument adapter", a set of three markers with a clamp, which attaches to any surgical instrument replacing the need for a separate probe. Different configurations of the markers on the adaptors allow for several instruments to be used simultaneously. The relative position of the instrument adapter markers to the tip of a surgical instrument with an adaptor attached can be calibrated using the calibration cone found at the juncture of the three arms of the reference frame. The "instrument calibration matrix" is used to measure the diameter and length of the instrument and the relative position of the instrument adapter markers to the tip. The system then tracks the surgical instrument in real time during the surgical procedure. The ability to use surgical instruments rather than a separate probe improves the efficiency of the system and allows for measurements to be taken continuously in real-time.

An early study (Gumprecht HK, et al, 1999) of the accuracies achievable using the VectorVision² system found a mean accuracy for registration of $1.4 \pm 0.51mm$. The intra-operative accuracies, including the mechanical accuracy, for target localization was found to be $4 \pm 1.4mm$. The study concluded that this was comparable to other systems in use. At the time of reporting, the system had been used successfully in 125 cases.

A recent study (Raabe A, et al, 2002) found the system accuracy to be $2.4 \pm 1.7mm$ in 34 successful cases employing laser scanning for patient registration. A maximum error of $9mm$ is reported.

Another system the StealthStation®, an early version of the StealthStation® Treon™ shown in figure 1.9, employs the FlashPoint Model 5000 tracking device (Image Guided Technologies, Inc, Boulder, Colorado). The FlashPoint consists of a three CCD camera array, a reference frame and probe. The reference frame and probe contain LED's. The three LED's are arranged in a straight line on the probe. The reference frame is attached to the Mayfield clamp and allows for the correction of movement of the patient. The coordinates of the LED's on the probe are measured and the coordinates of the tip extrapolated from them. The tip position is displayed relative to the corresponding

image data. The total technical error was measured under laboratory conditions and has been reported to be $0.55 \pm 0.64mm$ (Kaus M, 1997).

Figure 1.9 The StealthStation Treon from Medtronic

CHAPTER 2

Theory

2.1 Pattern Recognition

The photogrammetric system applies a pattern recognition algorithm to each of the stereo pair of images to extract the 2D coordinates of the markers that appear on the control frame and probe. The algorithm comprises two parts. The first is a circle detection algorithm (the markers are circular in shape), which scans the image for circular objects of a particular size. The second algorithm finds the centres of the circles using a centre of gravity technique. Both are described below.

The circle detection algorithm is derived from the method used by Kim HS and Kim JS (http://vivaldi.kaist.ac.kr/~iclab) and is based on the fact that the line perpendicular to and bisecting a chord on a circle passes through the centre of the circle. A simplified version of the routine, written in-house, utilises only a horizontal and vertical chord and the first edge on every side of the reference pixel.

The algorithm proceeds as follows: In the first instance the image is scanned from left to right and top to bottom. For each pixel above the threshold, the nearest pixel with a gray value below the threshold is found in the negative and positive directions for both x and y. In order to determine whether both chords are present, it is verified that the end coordinates of both chords are located in the image. The centre of the circle is found by determining the centres of both chords and finding the intersection of the perpendicular on the chord.

The radius is calculated to two points on the edge of the circle at positive x and y. The difference between the two radii must fall within a specified maximum to meet the criteria for a circle. The radius is compared to a set minimum to exclude small circles

and single bright pixels found in the image. Once the pixel is determined to meet the criteria for being located in a circle, a vote is cast for the centre of the circle.

Once this process has been repeated for all pixels in the image the centres with the highest number of votes are determined to be circles. The coordinates of the top twelve or three are then identified as the marker centres.

The second algorithm is used to refine the location of the marker centres identified with the first algorithm. For each marker centre that has been identified the maximum x- and y-coordinates and the minimum x- and y-coordinates in the circle are found and used to form a bounding box around it.

The centre is determined by using a weighting function to find the centre of gravity. Pixels above the threshold are given a higher weighting than pixels below the threshold. The following formulae are used:

$$X = \frac{\sum G * x}{\sum G} \quad \text{and} \quad Y = \frac{\sum G * y}{\sum G}, \tag{1}$$

$$G = {}^{g}\!/_{thr} \quad , \tag{2}$$

in which

g denotes the gray value of the pixel,

x and y are the pixel coordinates,

thr is the threshold of 240, and

X and Y are the centre of gravity coordinates.

Once the 2D coordinates of the centres of the markers have been determined, they are written to a text file. The files from each of the stereo pair of images are downloaded from the cameras to the laptop.

2.2 Photogrammetric Theory

The way in which a camera works may be modelled on the basis of perspective projection. Perspective projection is the transformation of data from a higher dimensional space to a lower dimensional space, in this case the 3D physical - to the 2D image space.

Perspective projection can be described using pinhole photography (figure 2.1) in which each point in the physical space reflects a ray of light that passes through the aperture or pinhole of the camera to form a point on the film in image space. The three points that define the light ray, namely the object point, the image point, and the pinhole aperture or perspective centre are collinear. The distance from the perspective centre to the image plane along the optical axis is known as the principal distance. The principal point of autocollimation is the point at which the optical axis, passing through the perspective centre, intersects the image plane. The image is made up of a bundle of light rays reflected from the object and its surrounds.

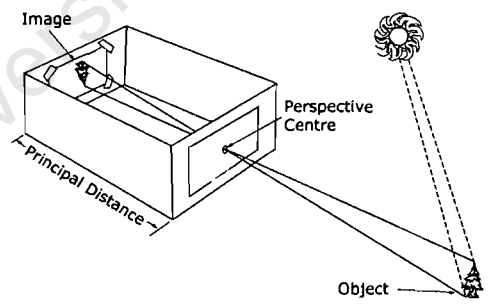

Figure 2.1 Illustration of the principle of pinhole photography. Light rays reflected off the object are projected through the pinhole aperture onto the back surface of the box where an image is formed. The aperture is known as the perspective centre and the perpendicular distance from the image plane to the perspective centre is the principal distance.

In a pinhole camera the depth of field is unlimited. The exposure time is however, very long. A sufficient amount of light needs to be let in through the aperture to shorten the exposure time. To maintain a sharp image with a short exposure time a refracting lens is required. This introduces lens distortion into the system. The distortion has two components: Radial and Decentring. The radial lens distortion refers to the radial displacement of the image from its theoretically correct position if the lens were distortionless. Decentring lens distortion is the geometric displacement of the image from this position.

The lens distortion along with the principle distance and principal point are known as the interior orientation parameters of a camera. They describe the internal geometric configuration of the camera and lens.

In a projective transformation from 3D to 2D space each object point corresponds to a unique image point. When projecting the 2D image back to 3D physical space each image point may be mapped to an infinite number of possible object points, so that two or more images are required for 3D reconstruction.

The two cameras used in a stereo-photogrammetric application function in a similar way to the human eye. When both cameras are focused on a specific point, the optical axes of the cameras converge at an angle called the parallactic angle (ϕ_1 in figure 2.2) and generate an image displacement d_1. Similarly when the cameras are focused on a point farther away, the optical axes converge forming a second parallactic angle (ϕ_2 in figure 2.2) and image displacement d_2. The distance between the two points and hence the depth of the object in space (figure 2.2) can be determined from the difference between the two angles ϕ_1 and ϕ_2. The magnitude of the parallactic angle is related to the image displacement.

If the cameras are positioned too close together the parallactic angles become very small and changes in the angles are difficult to discern, making depth difficult to judge.

Equivalently if the cameras are too far apart the parallactic angles become too large to judge the depth accurately.

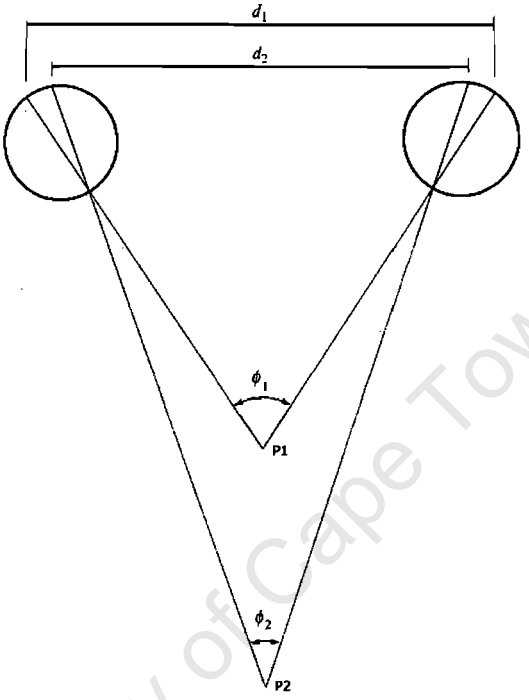

Figure 2.2 Illustration of the principle of parallax. The two parallactic angles ϕ_1 and ϕ_2 can be used to find the distance between points P1 and P2 and hence the depth of an object in space. d_1 and d_2, the image displacements, are closely related to the magnitude of ϕ_1 and ϕ_2.

The geometric configuration of the images relative to each other and to the physical space coordinate system is described by the parameters of exterior orientation (Mikhail, et al, 2001). The 3D reconstruction of points in the two images requires knowledge of the parameters of interior and exterior orientation. These are solved by camera calibration.

2.2.1 Camera Calibration

Camera calibration refers to the determination of the geometric parameters of lenses. The interior orientation is the mathematical description, by a set of parameters, of the path of a bundle of light rays through the lens to the image plane (Fryer, 1996). The exterior orientation describes the position and orientation of the bundle relative to the physical space coordinate system (Mikhail EM, et al, 2001).

The principal distance is often referred to as the focal length. The inclusion of fiducial marks or reseaux on the image plane provides an additional parameter for the correction of film deformation in analogue cameras. The fiducial marks are four or eight defined marks on the sides and or corners of the frame within the focal plane. Reseaux are a rectangular grid of calibrated marks imaged onto the negative, which allow a more precise correction for film deformation. The intersection of horizontal and vertical lines drawn between opposite fiducial pairs forms the fiducial origin. The distance x_p, y_p of the fiducial origin from the principal point forms the additional interior orientation parameters illustrated in figure 2.3.

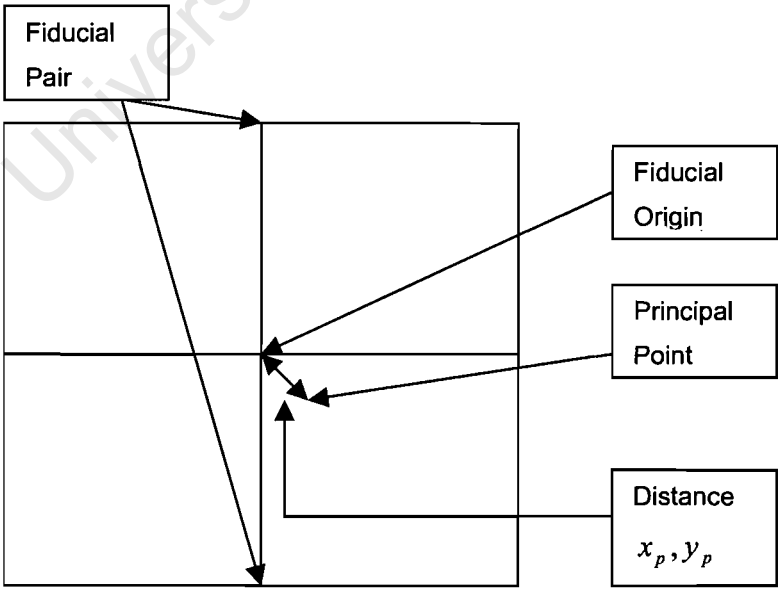

Figure 2.3 Illustration of the interior orientation parameters

The radial lens distortion can be described by the equation:

$$\delta r = K_1 r^3 + K_2 r^5 + K_3 r^7 \tag{3}$$

Where K_1, K_2 and K_3 are coefficients of radial distortion at infinity focus and

$$r^2 = (x - x_p)^2 + (y - y_p)^2, \tag{4}$$

in which x, y are the coordinates of a point in the image.

The decentring lens distortion can be described by the equations:

$$\Delta y_s = (1 - \frac{C}{S})[P_2(r^2 + 2(y - y_p)^2) + 2P_1(x - x_p)(y - y_p)] \tag{5}$$

$$\Delta x_s = (1 - \frac{C}{S})[P_1(r^2 + 2(x - x_p)^2) + 2P_2(x - x_p)(y - y_p)] \quad , \tag{6}$$

in which x, y are the fiducial coordinates of the image point, x_p, y_p is the distance of the principal point from the fiducial origin, r is the radial distance from the image centre to the image point, S is the distance from the lens to the physical plane on which the lens is focused, and C is the principal distance at S.

The interior and exterior orientation parameters are found using resection and intersection techniques. Resection refers to the determination of the position and orientation of the image in space. Intersection refers to calculation of the physical space coordinates of a point from its image space coordinates in two or more images. The two operations are combined in a triangulation where the physical coordinates and image orientation parameters are calculated simultaneously. Bundle adjustment, described in section 2.2.3, is an algorithm that uses triangulation. A further algorithm for

3D point reconstruction is the Direct Linear Transformation (DLT) described in section 2.2.2. These are two of the most widely used algorithms in photogrammetry.

Methods of camera calibration for determining the interior and exterior orientation parameters include On-the-job, Self and Analytical Plumb-line (Fryer JG, 1989).

On-the-job calibration determines the interior orientation parameters at the time of measurement. The object and object space control are imaged together. A control frame consisting of pre-coordinated coordinates can be used as an object space control. It is placed over the object prior to imaging. Figure 2.4 shows an object space control used for measurements of small objects. The use of an independent control is essential for a good outcome in on-the-job calibration.

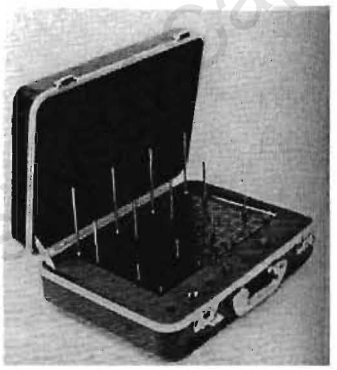

Figure 2.4 An Object Space Control used for measurements of small objects.

Self-calibration uses discrete targeted points on the object for object point determination and camera parameters. The collinearity equations modified by the addition of lens distortion parameters are used to solve the resultant bundle of equations simultaneously. Control targets with fixed coordinates are incorporated to derive the absolute orientation. Self-calibration does not require the use of external or independent control.

Analytical Plumb-line is often used as an independent check on self or to obtain trial values for a bundle adjustment. It works on the principle that a straight line in physical space will project as a straight line in image space. Departures from linearity are attributed to lens distortion. It only provides values for the radial and decentring distortion and not for the other interior orientation parameters. It provides ideal initial estimates for an iterative self-calibration technique employing bundle adjustment.

2.2.2 The Direct Linear Transformation (DLT)

The DLT as first proposed by Abdel-Aziz and Karara (1971) at the University of Illinois, is a mapping from image space to physical space. It transforms the 2D coordinates of a point visible on each of a number of images into the 3D coordinates of that point in real or physical space.

Initially the DLT was a linear transformation from image space to physical space based on the collinearity equations (9) and (10). The solution solved both the interior and exterior orientation parameters simultaneously. Image refinement parameters were not included. The DLT was later expanded to include parameters for lens distortion and film deformation. Karara and Abdel-Aziz (1974) found that only the first term in equation (3) needs to be taken into account for lens distortion. Thus the DLT is defined by:

$$x + (x - x_p)K_1 r^2 = \frac{L_1 X + L_2 Y + L_3 Z + L_4}{L_9 X + L_{10} Y + L_{11} Z + 1} \quad , \tag{7}$$

and

$$y + (y - y_p)K_1 r^2 = \frac{L_5 X + L_6 Y + L_7 Z + L_8}{L_9 X + L_{10} Y + L_{11} Z + 1} \tag{8}$$

where:

x and y are the coordinates of a point in the image,

x_p and y_p is the offset between the fiducial origin and the principal point in the image,

X, Y and Z are the 3D coordinates of the point in physical space,

L_1 to L_{11} denote the transformation parameters and

$(y - y_p)K_1 r^2$ is equivalent to the first term of lens distortion from equation (3)

A minimum of six control points are required to solve the twelve transformation parameters required for the mapping. The twelve parameters of the DLT are solved using a least squares adjustment. The mathematics is described in Appendix B.

The advantages of the DLT are that it is simple, it requires no initial approximations for the unknowns, and neither a calibrated camera nor fiducial marks or reseaux are required. A solution can still be obtained where a simultaneous bundle adjustment solution fails to converge due to a lack of reasonable initial approximations.

However, it requires a minimum of six 3D physical space control points that are well distributed in 3D space. The solution is less rigorous and can be of a lower accuracy compared with the bundle adjustment.

2.2.3 Bundle Adjustment

The bundle adjustment solution was developed by Brown in 1958 in Florida. It was originally developed for aerial photogrammetry as a block triangular adjustment and later applied to terrestrial work (Brown, 1971).

A bundle block adjustment establishes the position and orientation of each bundle of image rays converging at the perspective centre, using the rays in each bundle and the given ground control information. Resection and intersection techniques are combined

to simultaneously calculate the exterior and interior orientation parameters and point coordinates.

The bundle adjustment solution is based on the collinearity equations (Mikhail, et al, 2001):

$$x - x_o = f\left[\frac{m_{11}(X - X_L) + m_{12}(Y - Y_L) + m_{13}(Z - Z_L)}{m_{31}(X - X_L) + m_{32}(Y - Y_L) + m_{33}(Z - Z_L)}\right] \quad , \tag{9}$$

and

$$y - y_o = f\left[\frac{m_{21}(X - X_L) + m_{22}(Y - Y_L) + m_{23}(Z - Z_L)}{m_{31}(X - X_L) + m_{32}(Y - Y_L) + m_{33}(Z - Z_L)}\right] \tag{10}$$

where:

x and y are the coordinates of a point in the image,

x_p and y_p is the offset between the fiducial origin and the principal point in the image,

X, Y and Z are the 3D coordinates of the point in physical space,

X_L, Y_L and Z_L are the 3D coordinates of the perspective centre,

m_{11} to m_{33} are the elements of the rotation matrix.

A linearised least squares adjustment is used to evaluate the exterior and interior orientation, the camera calibration data and the physical space coordinates. f is solved using:

$$f = v + \dot{B}\dot{\delta} + \ddot{B}\ddot{\delta}, \tag{11}$$

where v is the image coordinate residuals, $\dot{\delta}$ contains the six exterior orientation parameters and $\ddot{\delta}$ contains the three physical space coordinates of the point. $\dot{B}$ and $\ddot{B}$ are the correction factors.

A self-calibrating bundle adjustment includes the interior orientation parameters as part of the unknowns to be solved for. It requires that the same camera be used for at least three well-distributed, convergent exposures and that fifty or more object points be included in the solution.

Bundle Adjustment has the advantage that it does not require calibration, although the inclusion of control points in an image provides a more rigorous solution. It has a high number of degrees of freedom, which increases the reliability of the solution. External control points are not required and a more reliable evaluation of camera calibration and interior orientation can be made than with straight resection and intersection techniques. The camera calibration parameters can vary from exposure to exposure (Cooper MAR, Robson S, 1996) since parameters are computed from every image.

It does, however, require good initial estimation values to ensure convergence. It takes longer and requires more computing power, since it involves large data sets and the computation of the inverses of large matrices.

The main distinction between the bundle adjustment and the DLT is that the DLT requires a 3D network of independently established control points, which if confined to a common plane causes the solution to become indeterminate.

2.2.4 The Rodrigues Matrix

The Rodrigues Matrix (Thompson, 1969) is used to transform coordinates from one 3D coordinate system to another where both systems have a common origin.

The following equation is used:

$$\begin{bmatrix} u \\ v \\ w \end{bmatrix} = R^T * \begin{bmatrix} x \\ y \\ z \end{bmatrix} \tag{12}$$

In (12) u, v and w are the coordinates in the new coordinate system of the point, whose coordinates in the original coordinate system are x, y, z. R^T is the Rodrigues matrix which describes three rotations around the coordinate axes, a scale transformation and a translation of the origin. A minimum of three reference points is required to solve for R^T. The mathematics is described in Appendix B.

This method is used to find the coordinates of the tip of the probe in SIIGNS. The coordinates of the three markers and the tip have been measured to an accuracy of $10\mu m$ in the x- and y-axes and 20 to $30\mu m$ in the z-axis using the Reflex Microscope (Scott PJ, 1981). The tip coordinates are transformed from the coordinate system of the microscope into theatre space using the three markers as common points.

The tip coordinates in 3D theatre space are then transformed into 2D CT space, with the z-coordinate determining the image slice number. The fiducial markers determine the transformation parameters between 3D theatre space and 2D CT space.

CHAPTER 3

Investigation of the Accuracies Achievable with the Metrograph

In order to design a cheaper, more robust alternative to tracking systems available commercially, a Reflex Metrograph, which was available in the laboratory, was used initially to perform 3D measurements.

This chapter describes the theoretical basis for this prototype navigator and presents the results and a discussion of its accuracy and repeatability.

3.1 Theoretical basis for the Prototype Navigator

The Prototype Navigator utilises the Reflex Metrograph (Scott, 1981) as the 3D measuring device. The system consisted of a pointer or probe (figure 3.1) held by the surgeon, the metrograph, and a transparent mirror positioned midway between the patient and the metrograph. The mirror consists of two identical sheets of glass with a semi-reflective surface in between.

The design of the Metrograph is based on the principle of "peppers ghost" (figure 3.2). Essentially, the image of the measuring mark, an LED, in the semi-reflective glass is positioned on the point of the object being measured. Its position in space is recorded with three rotary encoders. In this way contact with the patient is avoided and the space surrounding the patient is available to the surgeon. Figure 3.3 is a diagrammatic representation of the Metrograph and shows the measuring mark mounted on an arm that can be moved in 3D space. Scott (1981) reported accuracies for the Metrograph of $0.3mm$ in the depth readings and $0.1mm$ in the other two directions.

The 3D physical coordinates of the tip of the probe were computed from measurements of the physical coordinates of the three markers on the probe and the accurately known coordinates of the markers relative to the tip as measured using the Reflex Microscope (Scott, 1981) described in chapter 2 using a Rodrigues Transformation (Thompson, 1969). The computed theatre coordinates of the tip were transformed into the reference frame of the imaging modality, typically CT, and its position displayed on the nearest CT slice.

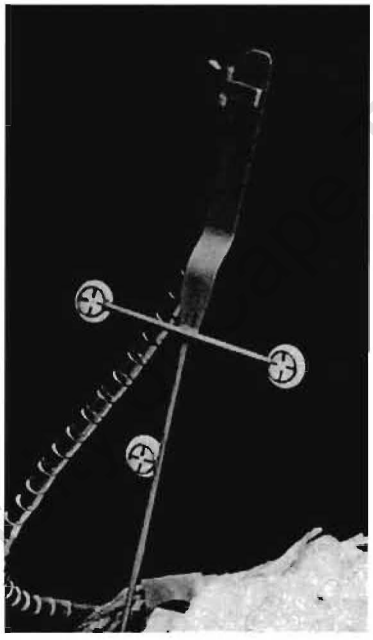

Figure 3.1: The pointer displaying the three markers clamped in place during surgery.

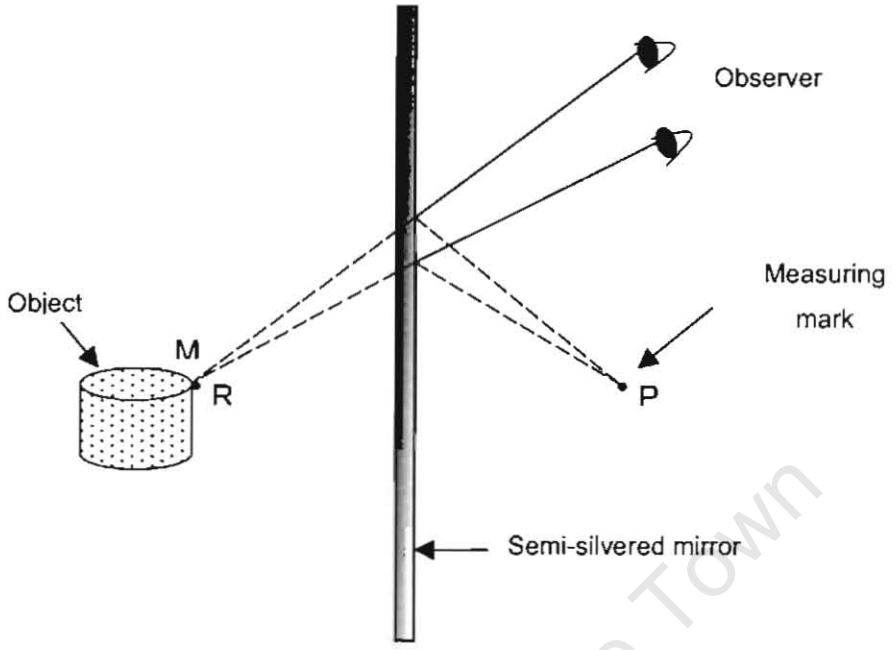

Figure 3.2: Diagram demonstrating the principle of Pepper's Ghost

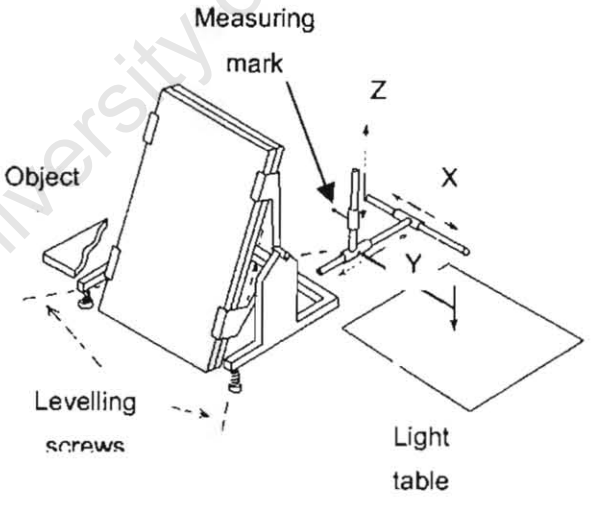

Figure 3.3: Diagram of the Metrograph

3.2 Accuracy of the Prototype Navigation System

3.2.1 Method of Investigation

The accuracies achievable with the Prototype Navigator were measured in two ways.

The first method followed the standard operational procedure described in section 6.1 but with the Metrograph replacing the cameras as the measuring device. The accuracies achievable with the Metrograph were investigated using a pumpkin phantom. A piece of wax was placed inside the pumpkin, representing a lesion in the brain. Four fiducial markers were placed around the top of the pumpkin. Three ball bearings were positioned on the wax as tumour points. The positions of the ball bearings could be accurately determined from the CT scans and used to assess the accuracy of intra-operative measurements of the tumour points.

The pumpkin containing the wax was scanned using CT scanning. The Metrograph was set-up in the same way as in theatre, with the transparent mirror mid way between it and the pumpkin. Patient Registration was then performed for the pumpkin. Each fiducial marker was measured using the probe. These coordinates together with the CT coordinates of the fiducials determined during digitisation were used to solve the Rodrigues parameters (Thompson, 1969) required to transform coordinates from physical space into CT space. Once the Rodrigues parameters were known the fiducials and tumour points were measured, transformed into CT space, and the results compared to the coordinates obtained from digitisation of the CT scans.

The second method of investigation utilised a phantom consisting of 15 points arranged randomly with different heights and at different positions in a 3D volume. The coordinates of the points had been measured using the Reflex Microscope (Scott, 1981) to an accuracy of $10\mu m$ in the x- and y-directions and 20 to $30\mu m$ in the z-direction. The points were re-measured using the probe and Reflex Metrograph combination and then transformed into the coordinate system of the microscope using the Rodrigues

Transformation. The transformed coordinates were compared with the previously calibrated coordinates of the points on the phantom and the errors computed in order to determine the accuracy achievable with the system. In order to assess the repeatability, the same point was re-measured a number of times for a couple of different points. The absolute maximum difference between repeated measurements was determined within each set. The mean of these absolute maximum differences for the different sets yields a value for the repeatability.

3.2.2 Results

3.2.2.1 Accuracy

The accuracy of the system as assessed from measurements of the fiducials and lesion points using the first method described above are presented in table 3.1. With the second method a number of independent sets of data were used to assess the accuracy. The results are presented in table 3.2.

Table 3.1 Errors obtained with the Prototype Navigator using a pumpkin with a lesion comprising a lump of wax. The normal procedure for a surgical operation was followed using the Prototype Navigator. The combined mean refers to the mean of all the points measured.

		Δx (mm)	Δy (mm)	Δz (mm)	RMSE (mm)
Fiducials	Mean	1.6	1.0	1.1	2.4
	Std Dev	0.9	0.5	0.7	0.5
	Max	2.7	1.6	1.8	3.0
Lesion	Mean	1.3	1.0	1.3	2.4
	Std Dev	0.8	0.8	0.7	0.5
	Max	2.2	1.9	2.1	3.0
Combined	Mean	1.4	1.0	1.2	2.4
	Std Dev	0.8	0.6	0.7	0.5
	Max	2.7	1.9	2.1	3.0

Table 3.2 Errors obtained with the Prototype Navigator using a phantom consisting of 15 points randomly positioned in a 3D volume. Comparison of Metrograph results with previously calibrated data.

	Δx (mm)	Δy (mm)	Δz (mm)	RMSE
Mean	1.6	1.4	0.5	2.4
Std Dev	0.7	0.8	0.4	0.7
Max	2.8	2.9	1.3	3.5

In method one the accuracy was investigated using a pumpkin containing fiducial markers and tumour points. The mean and standard deviation (Std Dev) of the errors were found to be $1.4 \pm 0.8mm$ in the x-axis, $1.0 \pm 0.6mm$ in the y-axis and $1.2 \pm 0.7mm$ in the z-axis. The mean and standard deviation of the root mean square error (RMSE) for each measurement were found to be $2.4 \pm 0.5mm$ with an absolute maximum difference (Max) of $3.0mm$. With the second method, a phantom consisting of 15 points whose coordinates are accurately known was measured. The mean and standard deviation of the errors were found to be $1.6 \pm 0.7mm$ in the x-axis, $1.4 \pm 0.8mm$ in the y-axis and

$0.5 \pm 0.4mm$ in the z-axis. The mean and standard deviation of the RMSE were found to be $2.4 \pm 0.7mm$ with an absolute maximum distance of $3.5mm$.

The mean error in the x- and y-axes are smaller in method one using the pumpkin, but the mean error in the z-axis is larger. The RMSE are similar.

3.2.2.2 Repeatability

The repeatability of the system was ascertained by repeatedly measuring a number of points on the phantom. The results are presented in table 3.3. The absolute maximum difference between measurements in the x-, y- and z-axes were found and the mean and standard deviation of these maximums computed. In addition, the root mean square error was computed for each repetition and the absolute maximum difference between these determined. The mean and standard deviation of the absolute maximum difference was computed.

Table 3.3 Repeatability of the Prototype Navigator as determined from a phantom study. A number of points positioned in 3D space were measured repeatedly and the differences between measurements assessed.

	Δx (mm)	Δy (mm)	Δz (mm)	RMSE (mm)
Mean	0.4	0.2	1.2	1.3
Std Dev	0.3	0.1	0.4	0.5
Max	1.2	0.3	1.8	2.0

The mean of the absolute maximum differences was found to be $0.4 \pm 0.3mm$ in the x-axis, $0.2 \pm 0.1mm$ in the y-axis and $1.2 \pm 0.4mm$ in the z-axis. The mean and standard deviation of the RMSE of the absolute maximum difference between repeated

measurements of the same point was found to be $1.3 \pm 0.5mm$ while the absolute maximum difference between two measurements of the same point was $2.0mm$.

3.3 Discussion

Method one determined the system accuracy to be $2.4 \pm 0.5mm$ with a maximum error of $3.0mm$. Method two determined the accuracy to be $2.4 \pm 0.7mm$ with a maximum error of $3.5mm$. These values reflect the mean and standard deviation of the RMSE errors between measurements of the 3D coordinates of points on the phantom and the accurately known coordinates of the points. These are similar. In comparison the procedural accuracy of commercial systems is higher and ranges from $1.03mm$ for the Magellan Frameless Stereotactic System (Zaaroor, et al, 2001) to $2.26 \pm 0.83mm$ for the SMN Pointer (Benardete, et al, 2001).

The mean error found in the x- and y-axes was $1.4 \pm 0.8mm$ and $1.0 \pm 0.6mm$ respectively using the first method, which was lower than was found using the second method, where the mean error was $1.6 \pm 0.7mm$ and $1.4 \pm 0.8mm$ for the x and y-axes, respectively. The mean error found in the z-axis was lower using the second method, $0.5 \pm 0.4mm$, than for the first method where the error was $1.2 \pm 0.7mm$. The Reflex Metrograph has a measuring resolution of $0.3mm$ in the depth readings and $0.1mm$ spread in the other two directions, therefore the measured errors are very high and may be affected by other sources of error, as described below.

There are several contributing sources of error in the investigation. Accuracies of $1.5mm$ have been reported for the CT scanner used in this study. Furthermore, a single measurement of the tip of the pointer requires three markers to be measured. For each measurement the reflection of the LED has to be positioned accurately in the centre of the marker. The measurement is very subjective, especially when determining the depth of the marker centre. In the first method, a pumpkin was utilised as the phantom, which lasts up to four days before it starts to decay. As a result all tests and

measurements must be performed in this period. Errors may be introduced into the measurements by the shift in position of the wax tumour as the pumpkin decays.

The repeatability of the system was determined to be $1.3 \pm 0.5mm$. Compared to systems commonly in use, this is a low precision. The precision or repeatability of commercial systems has been reported as $0.2mm$ for the ISG Viewing Wand and $0.36mm$ for the SMN Pointer (Benardete, et al, 2001).

The Metrograph-based navigator has several notable limitations. Positioning the reflection of the LED alternately on the centres of each of three markers by sight is required for a single measurement. This requires a high level of concentration, a finite time (roughly a minute), and experience in order to position the LED accurately. In addition the equipment is bulky and difficult to transport. The mirror is positioned close to the bed in the space in which the nurses move around. If the mirror is bumped the patient needs to be re-registered using the burr holes drilled during the craniotomy. Since the fiducials are removed after patient registration, re-registration will not be possible if movement of the mirror or patient occurs between this time and registration of the burr holes (refer to Section 6.1).

Despite these limitations, an experienced professional can achieve good accuracy and the Prototype Navigator has been successfully used in several operations.

CHAPTER 4

Feasibility of an Ultrasound System as the Three-Dimensional Measuring Device in the Neurosurgical Guidance System

Ultrasound provides a viable option for the replacement of the technology used in the 3D measuring device of the neurosurgical guidance system. One such device is the Zebris System manufactured by Zebris Medizintechnik GmbH (Isny—Tübingen, Germany) (http://www.zebris.de/). Zebris is an ultrasound 3D positioning system designed for use with an electro encephalogram (EEG). The system employs the motion analyser, CMS30P, to measure the 3D coordinates of markers/electrodes positioned around a patient's head. The system accuracy is specified as having a resolution of 0.1mm in the position measurement with +/- 0.26mm maximum deviation.

The feasibility of replacing the Metrograph with the Zebris system as the 3D measuring device in the Neurosurgical Guidance System has been investigated in this chapter.

4.1 The Zebris System

The system (figure 4.1) consists of a receiver comprising three ultrasonic microphones arranged in a fixed orientation relative to each other, and a pointer with two ultrasonic transmitters separated by a fixed distance and fixed relative to the tip of the pointer. The transmitters are set to continuously emit a pulse. The three dimensional coordinates of a point are calculated by the triangulation of these pulses via the receiver. Measurements are obtained by positioning the tip of the pointer on the marker or point to be measured and depressing the button on the pointer as illustrated in figure 4.1. It is important that there is no obstruction between the transmitters on the pointer and the receiver.

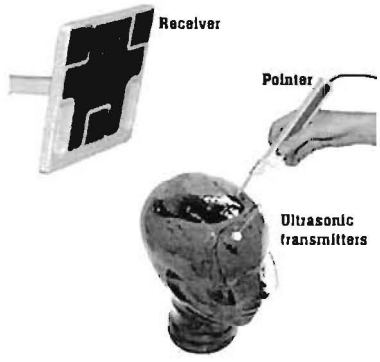

Figure 4.1: The Zebris ultrasound system

Three ultrasonic transmitters are placed at pre-defined positions on the patients face and are set to continuously emit a pulse. The positions of the transmitters (S1, S2 and S3 in figure 4.2) define a static coordinate system for the head called the *cross coordinate system*. The use of this coordinate system allows the Zebris system to correct for any movement made by the patient. Three anatomical features, usually the tragi of each ear and the bridge of the nose, are measured in reference to the *cross coordinate system*. These define the *head coordinate system*. The surface points or markers are measured in relation to this coordinate system and can therefore be given an anatomical reference.

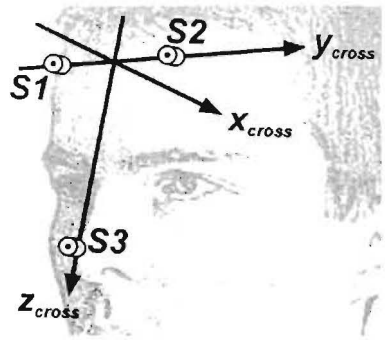

Figure 4.2 Three ultrasound transmitters, S1, S2, S3 define the cross coordinate system

4.2 Feasibility of the Zebris System

The following areas were investigated:

- Accuracy of the measurements
- Repeatability
- The effect of movement on the repeatability
- Optimal marker configuration
- The achievable depth within the skull with the pointer dimensions
- The practicalities of using the system with or without the transducers, which define the static head coordinate system.

The transducers placed on the patient would pose a problem in neurosurgical applications since the patient is completely covered in drapes during the operation and the transducers require line-of-sight. The surgical space is the only area exposed. Since the patient is anaesthetised and their head clamped in position for the duration of the operation, movement is not likely so that the transducers are not a requirement. The operation of the Zebris system without them has therefore been investigated.

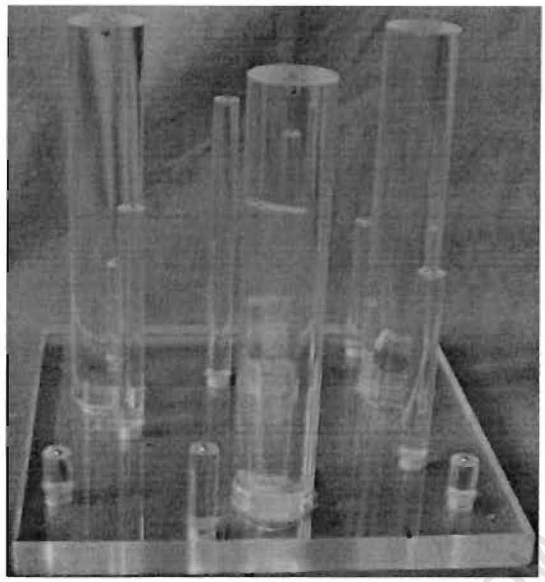

Figure 4.3 The phantom consisting of 15 points randomly positioned in a 3D volume. The coordinates of these points have been measured to an accuracy of $10\mu m$ *in the x and y-axes and* $20\mu m$ *to* $30\mu m$ *in the z-axis using the Reflex Microscope (Scott, 1981).*

4.2.1 Method

The Zebris system was positioned with the stand on which the receiver is mounted, clamped to a desk and a phantom placed within a metre of the receiver. The motion analyser connects to the receiver, transducers and pointer via cables. The phantom, shown in figure 4.3, consists of 15 points arranged at different heights and positions in a 3D volume and has been accurately measured using the Reflex Microscope (Scott, 1981) as described in chapter 2. The motion analyser was connected to a laptop containing the Zebris software ElGuide. The user interface is shown in figure 4.4. The three sonic transducers were fixed to the phantom in a configuration similar to the recommended facial positions, shown in the top right corner of figure 4.4 in the picture called patient marker. The software requires the left and right tragi of the ears and the nasion to be measured for defining the head coordinate system. Points on the phantom were selected to replace these anatomical features. The option *Collect Surface Points*

(figure 4.4) of EIGuide was used to measure the 3D position of the points on the phantom. The point positions were saved to a file as both polar and Cartesian coordinates.

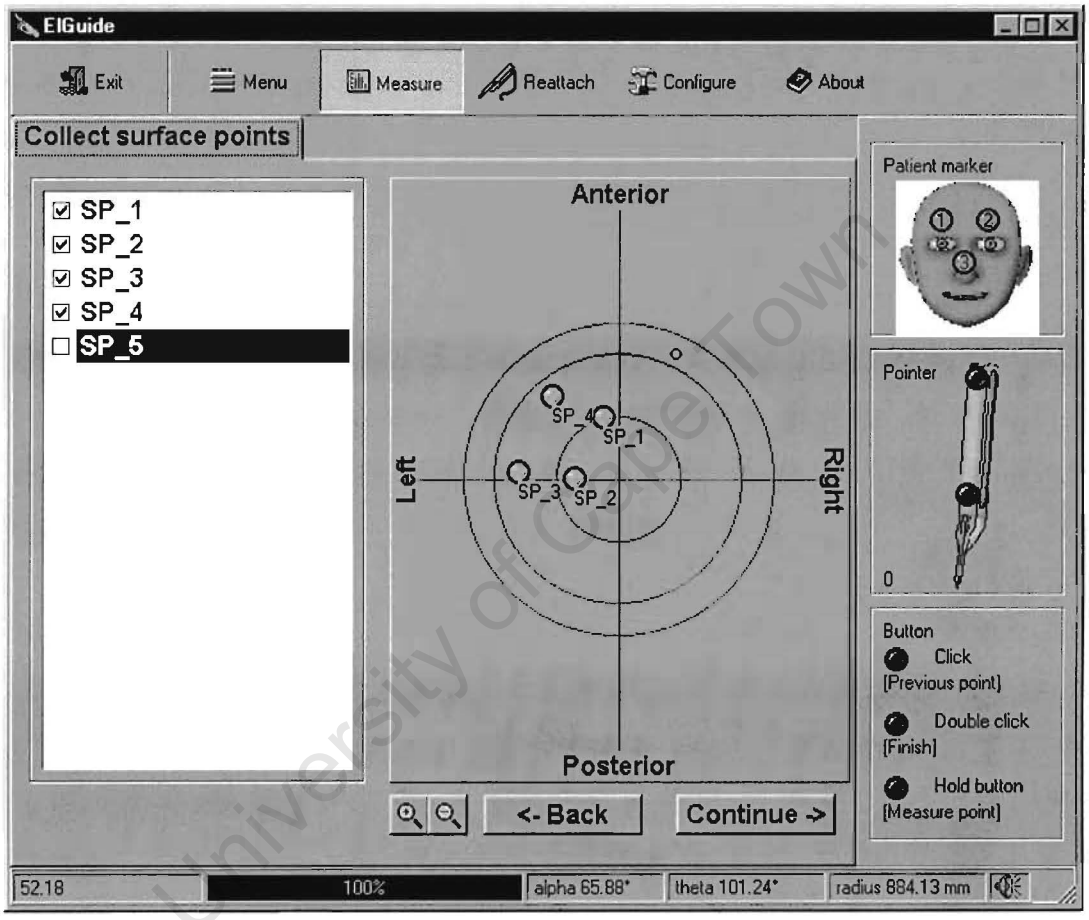

Figure 4.4 The Zebris software user interface: EIGuide.

4.2.2 Results

4.2.2.1 Accuracy

The 3D coordinates of all the points on the phantom were measured. The Rodrigues Transformation (Thompson, 1969) was used to find the Rodrigues parameters to transform the measured coordinates into the coordinate system of the phantom. The transformed coordinates were then compared to the known coordinates of the phantom and the mean and standard deviation of the errors computed. The absolute values of the errors were used. The procedure was repeated three times independently.

The table below shows the results of the investigation.

Table 4.1 Errors obtained with the Zebris system

Set		Δx (mm)	Δy (mm)	Δz (mm)	RMSE (mm)
1	Mean	1.6	1.2	1.2	2.5
	Std Dev	0.9	0.7	0.7	0.9
	Max	3.5	2.7	2.6	4.5
2	Mean	1.6	1.4	0.7	2.5
	Std Dev	1.0	1.0	0.8	1.0
	Max	3.2	3.8	2.7	4.2
3	Mean	0.9	0.9	1.4	2.2
	Std Dev	0.7	0.6	1.2	1.0
	Max	2.3	2.2	3.4	4.1
Ave	Mean	1.4	1.2	1.1	2.4
	Std Dev	0.9	0.8	0.9	1.0
	Max	3.5	3.8	3.4	4.5

The mean and standard deviation of the errors was found to be $1.4 \pm 0.9mm$ in the x-axis, $1.2 \pm 0.8mm$ in the y-axis and $1.1 \pm 0.9mm$ in the z-axis. The root mean square

error is a measure of the difference between the measured and accurately known coordinates of the points on the phantom. This was found to be $2.4 \pm 1.0mm$ with a maximum difference of $4.5mm$.

4.2.2.2 Repeatability

The repeatability of the system was assessed by repeatedly measuring a number of the points on the phantom. The absolute maximum difference in the x-, y- and z-axes and the root mean square error were computed for each point (i.e. each set of measurements) and the mean and standard deviation computed from the absolute maximum differences obtained for the different sets.

Table 4.2 shows the results for the repeatability.

Table 4.2 Results of the investigation into the repeatability of the Zebris system

	Δx (mm)	Δy (mm)	Δz (mm)	RMSE (mm)
Mean	3.1	2.1	2.7	4.3
Std Dev	0.8	1.3	2.1	1.7
Max	4.4	4.5	6.9	8.4

The mean and standard deviation was found to be $3.1 \pm 0.8mm$ in the x-axis, $2.1 \pm 1.3mm$ in the y-axis and $2.7 \pm 2.1mm$ in the z-axis. The root mean square error in measurements of the same point was $4.3 \pm 1.7mm$ while the maximum difference between measurements of the same point was $8.4mm$.

4.2.2.3 The Effect of Movement on the Repeatability

The effect of movement on the repeatability was investigated by repeatedly measuring a number of points on the phantom. The position of the phantom was changed before each measurement. The absolute maximum difference in the x-, y- and z-axes and the root mean square error were computed. The mean and standard deviation of the maximum differences were computed.

Table 4.3 shows the results for the effect of movement on the repeatability of the Zebris system.

Table 4.3 Effect of movement on the repeatability

	Δx (mm)	Δy (mm)	Δz (mm)	RMSE (mm)
Mean	2.0	1.1	1.0	2.3
Std Dev	0.8	0.5	0.5	0.9
Max	2.9	1.7	1.3	3.4

The mean and standard deviation of the absolute maximum difference between measurements was found to be $2.0 \pm 0.8mm$ in the x-axis, $1.1 \pm 0.5mm$ in the y-axis and $1.0 \pm 0.5mm$ in the z-axis. The mean and standard deviation of the difference between measurements is $2.3 \pm 0.9mm$ while the absolute maximum difference is $3.4mm$.

The poor repeatability, presented in this section, indicated that the system would not be feasible for application in neurosurgery and therefore the achievable depth, optimal marker configuration and use of the transducers were not investigated.

4.3 Discussion

The investigation determined the errors obtained with the Zebris system to be $2.4 \pm 1.0mm$. This is comparable with the error of $2.4 \pm 0.7mm$ reported in chapter 3 for the Metrograph. These values are, however, higher than the errors reported for neurosurgical guidance systems currently in use, which range from $1.03mm$ for the Magellan Frameless Stereotactic System (Zaaroor, et al, 2001) to $2.26 \pm 0.83mm$ for the SMN Pointer (Benardete, et al, 2001).

The repeatability of the system was determined using the mean of the absolute maximum difference between measurements of the same point and was found to be $4.3 \pm 1.7mm$. The maximum difference between two measurements of the same point was $8.4mm$. The precision of commercial systems has been reported as $0.2mm$ for the ISG Viewing Wand and $0.36mm$ for the SMN Pointer (Benardete, et al, 2001). The investigation revealed that the angle at which the pointer is directed to the marker affects the accuracy of the measurement. Repeatedly measuring a point without varying the angle improved the results. This indicates a lack of reliability in the system.

The investigation into the effect of movement on repeatability essentially tested the effectiveness of the transducers fixed to the patient, or phantom in this case. The repeatability while moving the phantom was determined to be $2.3 \pm 0.9mm$, which is lower than the repeatability determined for the system. However, a smaller sample size was used, which would affect the mean error.

There are several issues that may have contributed to the magnitude of the errors found in the investigation into the system accuracy. The pointer employs 2 transmitters in a linear configuration with the tip to extrapolate the position of the tip. A triangular configuration of 3 markers provides a more precise transformation to compute the coordinates of the tip (refer to chapter 2). Measurements are recorded by holding down a button on the pointer for a few seconds. This introduces movement into the system, affecting the accuracy of the measurement. There are several factors that affect the

propagation of ultrasound, such as temperature, wind, distance and reflections of the ultrasonic waves. The software incorporates a temperature sensor to reduce the effects of temperature on the system. The distance between the pointer and the receiver should be less than 1.5m; at greater distances the accuracy decreases, as shown by Henry Chateau, 2003 using the Zebris CMS-HS, a kinematic analysis system.

A further drawback of the system is the cables which connect the pointer and transducers to the motion analyser.

CHAPTER 5

Components of the Stereo-Photogrammetric System

The surgical procedure followed using the proposed stereo-photogrammetric system is described in chapter 6. The system consists of the following components: Two smart cameras, the camera enclosure and stand (figure 5.4), the control frame (figure 5.7), a probe (figure 5.9), software and a laptop. Although the smart cameras are contained within the enclosure, they are treated as a separate entity given that they play a significant role in the functioning of the system. The software comprises two components: an imaging component which runs on the smart cameras and the graphical user interface that runs on the laptop. The laptop connects to the cameras via an Ethernet link.

The set up, illustrated in figure 5.1, is as follows: The two smart cameras are mounted in the enclosure at a fixed distance of $0.4m$ apart. The enclosure is mounted on the stand at a height of $0.8m$ above the surgical table and $1.5m$ from the patient's head. The cameras are focused on the operating space, which has been calibrated using the control frame. This is achieved by briefly holding the control frame above the patient's head at the start of the surgical procedure and simultaneously taking a pair of images. After calibration, the probe is used whenever a measurement is required.

This chapter introduces the third three-dimensional measuring device proposed for the neurosurgical navigation system. The components of the stereo-photogrammetric system are explained and their design issues described.

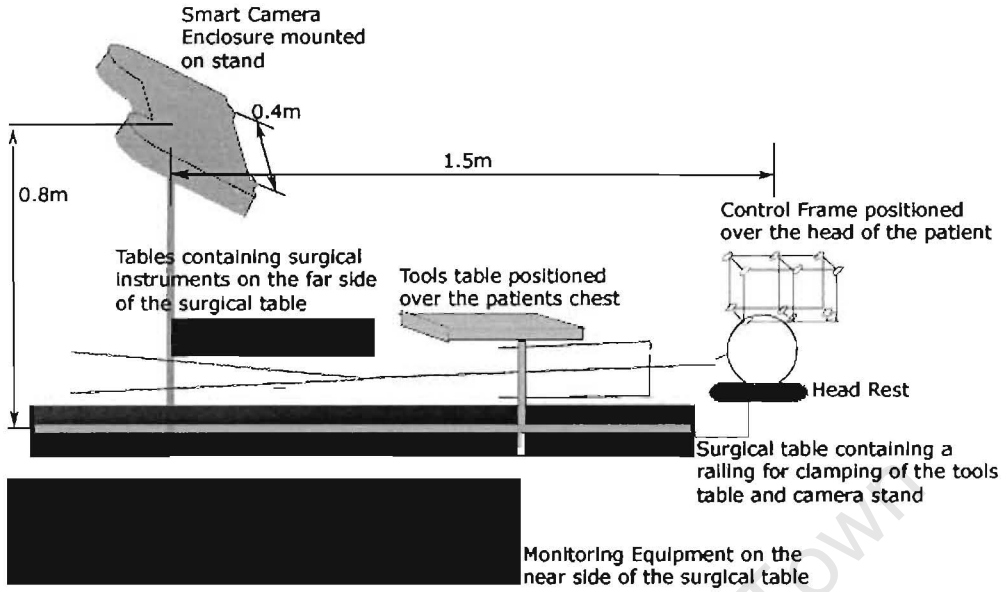

Figure 5.1 Diagram illustrating the set-up of the components of the stereo-photogrammetric system.

5.1 The Smart Cameras

Electronic Development House (EDH) (Stellenbosch, South Africa), designed the smart cameras used in the image-guided neurosurgical system. The current version of the cameras is still a prototype (figure 5.2). They each contain a StrongArm SA1110 206MHz processor running a version of Debian Linux adapted for the cameras. Each camera contains a Sony CCD area imager, with a 512×492 pixel resolution providing a 256 level grayscale image. The processor connects to the imager via Camera Link (http://www.pulnix.com/CameraLink/CL-prods.html). Each camera has its own IP address for use over a network. Detailed camera specifications are provided in Appendix A.

The lenses used on the cameras are Yamano $16mm$, manual iris lenses. The lenses are placed $400mm$ apart, which was found to provide greatest 3D reconstruction accuracy.

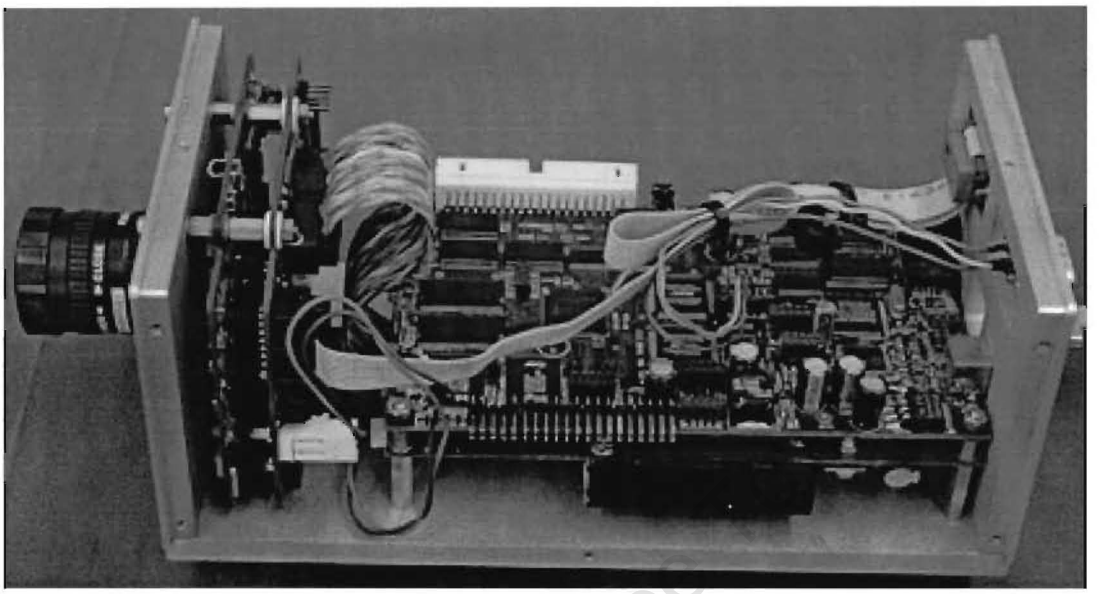

Figure 5.2 The smart camera

5.2 The Camera Enclosure and Stand

As illustrated in figure 5.3, the camera enclosure contains the two cameras, their power supply unit and the hub. The hub is a 10 Mbps 8 port Ethernet hub, which links the two cameras and the laptop across a network. The enclosure provides access to two of the Ethernet ports, one is an uplink for connection to a network, and the second port connects to the laptop. A board of infrared LEDs is mounted externally on the enclosure between the two cameras. It replaces the original LED ring flashes, which hampered the focusing of the lenses. The cameras are triggered from the laptop and are not completely synchronous but trigger tenths of a millisecond apart. For this reason each camera is synchronised with half the LEDs. The LEDs are divided between the cameras so that every second column flashes with camera A and every other column with camera B. This division allows a greater coverage of the area being focused on and therefore a greater reflection value.

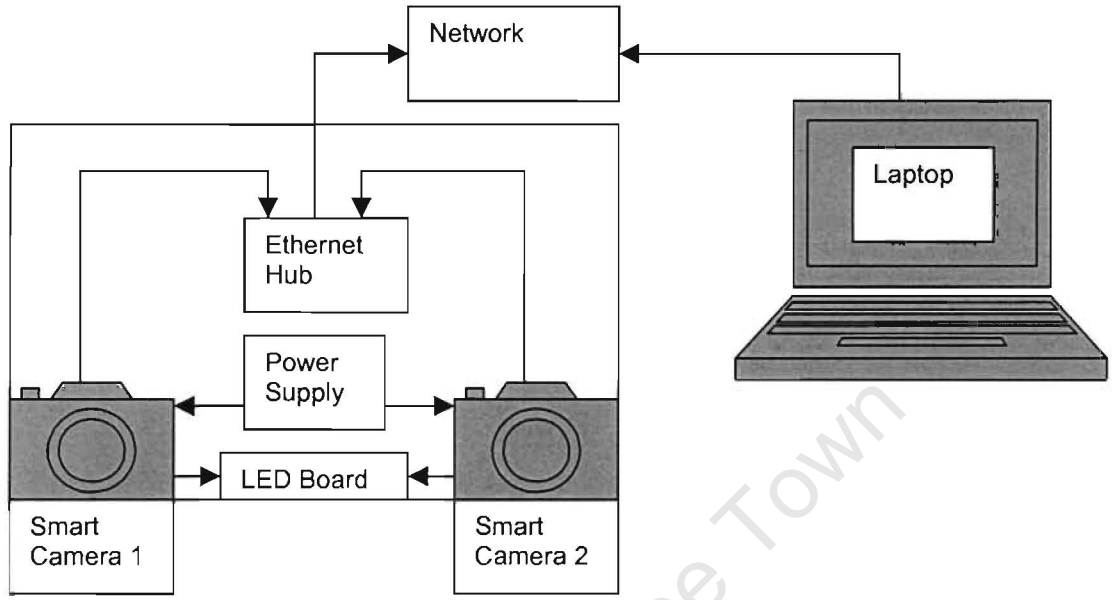

Figure 5.3 Diagram showing the connections between the cameras and laptop

One of the design requirements of the enclosure was that the cameras had to be the correct distance apart in order to most accurately ascertain the depth of objects in the 2D images. The method for determining this distance is described in section 5.2.1. A wheel on the underside of the enclosure adjusts the angle of the cameras allowing them to focus on an object at a distance of $1m$ to $7m's$.

One limitation of photogrammetry is the line-of-sight requirement. The area surrounding the surgical table is mostly occupied. The monitoring systems and the anaesthetist are on one side of the surgical table. The other side contains tables holding the surgical instruments; the nurses also stand in this area. The surgeons stand at the head of the table. The lights are positioned directly above the area where they are operating. The tools table is positioned over the chest of the patient. This standard configuration of theatre space (figure 5.1) leaves the area at the foot of or above the table clear, which is the reason why it was decided to mount the camera enclosure in this area.

The table or bed has a railing on either side for clamps to run along. The stand for the cameras is clamped to this railing on either side of the table near its foot. The stand contains a standard tripod mount on which the camera enclosure is mounted (figure 5.4(b)) above the bed. Alternatively, it may be mounted on a tripod next to the bed.

As shown in figure 5.4(b) the stand consists of two uprights connected by cross bars at the top and lower down. At the lower end of each upright there is a $5mm$ raised ring, $45mm$ from the end. This ring provides a stop when positioning the upright in the clamp.

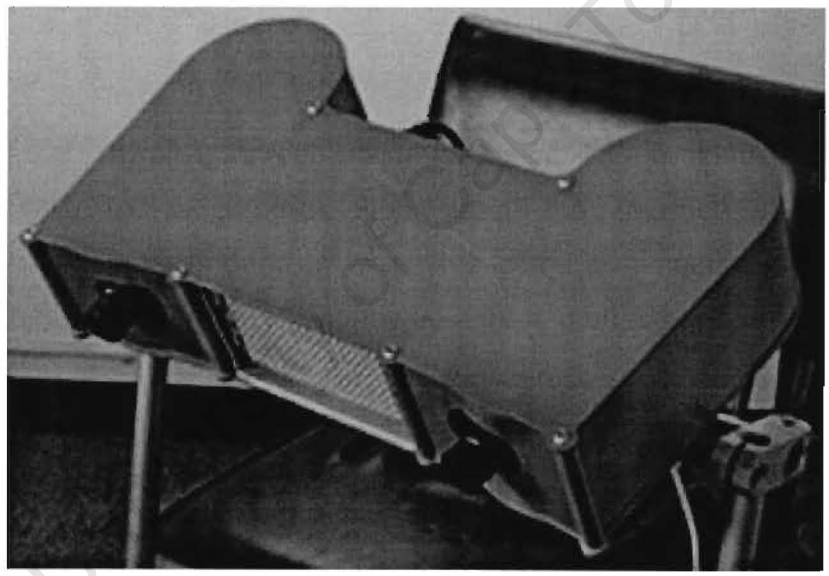

(a)

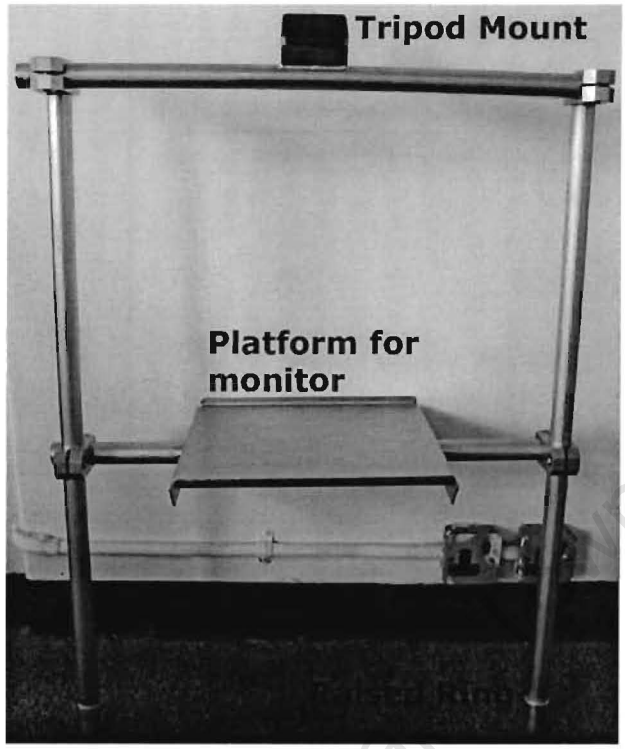

(b)

Figure 5.4 (a) The camera enclosure and (b) stand

Midway along the cross bar is a tripod mount for attachment of the enclosure to the stand. The cross bar can be rotated by loosening allan bolts on either side allowing it to be tilted forwards and backwards. It can also be angled to either side by adjusting the tripod mount. A second cross bar containing a platform can be attached to the uprights for positioning a monitor or laptop.

Lochner Design produced the design of the enclosure and stand. Figure 5.5 shows the arrangement of hardware within the enclosure.

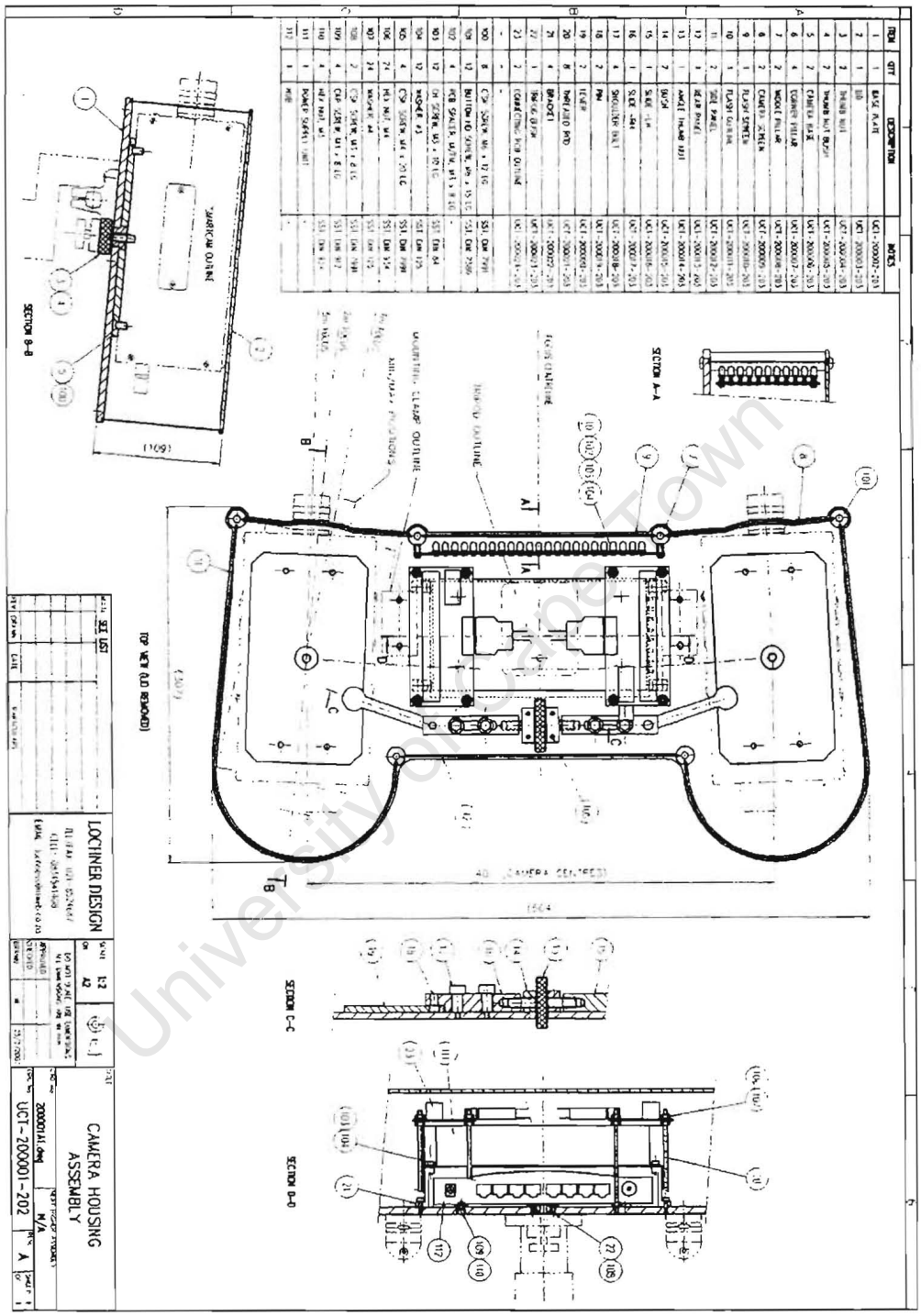

Figure 5.5 Configuration of the hardware within the camera enclosure

5.2.1 Determination of Optimal Distance between Cameras

The distance between the lenses of the two cameras affects the accuracy of the DLT. Accurate extrapolation of the depth measurement from a stereo pair of images cannot be achieved if the cameras are too close or too far apart, as mentioned in chapter 2.

The optimum distance between the cameras was determined using a single camera, due to the late completion and arrival of the second camera. The frame was placed on the floor. The camera was positioned directly facing the frame at a distance of $1.5m$, corresponding to the distance from the patient headrest to the position of the camera stand along the surface of the operating table. The camera was raised $0.8m$ above the floor, equivalent to the height of the camera position above the operating table.

Measurements were taken $250mm$ to the left of this position parallel to the frame and $250mm$ to the right of this position along the same line, replicating images from the left and right cameras. The camera was triggered at $25mm$ intervals as it was moved along this line. A stereo-pair was formed between the left and right images taken at equal distances from the centre position. The smallest distance between the cameras was $200mm$ and the largest distance was $500mm$.

The pattern recognition algorithm was applied to each of the images and the 2D coordinates obtained from each stereo-pair were used to solve the transformation parameters of the DLT (described in chapter 2). The 3D coordinates of the frame were then computed using the parameters. These were compared to the accurately known 3D coordinates of the frame. Table 5.1 shows a sample of the data for the case when the separation was $400mm$.

The errors from each stereo-pair were compared to find the lowest errors, which would present the optimal distance between the cameras.

5.2.1.1 Results and Conclusion

A sample set of the data for the method described above is presented below.

Table 5.1. The 2D coordinates of the frame identified from the left and right images; the 3D coordinates found using the DLT compared with the known 3D coordinates of the frame.

2D coordinates at 400mm				3D coordinates at 400mm					
Left Image		Right Image		Calibrated			Measured		
x (mm)	y (mm)	x (mm)	y (mm)	x (mm)	y (mm)	z (mm)	x (mm)	y (mm)	z (mm)
100.5	130.0	116.0	137.0	-15.5	163.9	0.9	-15.3	163.7	1.4
101.0	169.0	100.0	175.0	-12.0	142.8	-92.9	-12.0	142.8	-92.4
99.5	214.0	80.0	220.0	-10.2	120.4	-185.6	-10.4	120.8	-186.2
131.5	268.5	160.0	272.5	17.3	26.5	26.2	17.0	26.5	25.4
132.5	315.0	146.0	318.0	19.4	5.1	-67.1	19.1	4.8	-67.4
99.5	364.0	99.0	367.0	-8.4	-17.2	-153.1	-7.9	-17.3	-152.2
386.5	137.0	402.5	131.0	254.0	165.7	7.2	254.0	165.6	6.9
403.5	174.5	403.0	169.0	256.4	145.0	-86.7	256.1	145.1	-85.4
421.0	219.0	402.0	213.5	256.8	123.2	-176.5	257.1	123.0	-177.6
345.5	270.5	375.0	268.0	224.9	28.8	32.1	225.2	29.0	32.3
359.5	316.0	373.5	313.5	227.1	7.7	-61.5	227.3	8.0	-62.1
408.0	366.0	407.5	363.5	260.1	-13.8	-148.5	259.8	-14.1	-147.9

Table 5.1 presents a sample set of 2D coordinates found by applying the pattern recognition algorithm to the stereo-pair of images taken with a separation of $400mm$. The 2D coordinates were converted to 3D coordinates using the DLT. The measured coordinates were compared to the accurately known coordinates of the frame. The absolute differences were found and the mean and standard deviation computed. The results are presented in table 5.2.

Table 5.2. Mean differences and standard deviation of the errors found in the x-, y- and z-directions for different camera separations. The maximum absolute difference is presented along with the root mean square error (RMSE) and standard deviation.

Camera Distance (mm)	Δx (mm)			Δy (mm)			Δz (mm)			RMSE (mm)	
	Mean	Std Dev	Max	Mean	Std Dev	Max	Mean	Std Dev	Max	Mean	Std Dev
200	0.37	0.24	0.96	0.63	0.67	2.54	2.11	1.83	6.47	2.32	1.86
250	0.27	0.21	0.87	0.30	0.22	1.03	0.94	0.72	3.36	1.09	0.68
300	0.37	0.28	1.06	0.45	0.40	1.66	1.51	1.44	5.79	1.70	1.43
350	0.26	0.20	0.90	0.35	0.31	1.74	1.44	0.95	4.39	1.55	0.95
400	0.30	0.19	0.97	0.32	0.23	0.94	0.91	0.68	2.75	1.08	0.63
450	0.31	0.28	1.29	0.34	0.29	1.81	1.18	0.98	4.72	1.33	0.99
500	0.34	0.26	1.11	0.42	0.38	1.86	1.53	1.21	4.40	1.69	1.19
550	0.29	0.22	0.98	0.34	0.29	1.36	1.50	1.08	5.18	1.62	1.07
600	0.28	0.22	0.91	0.27	0.22	1.09	1.16	0.76	3.20	1.27	0.73

The results presented in the table show that at a distance between the cameras of $400mm$ the RMSE of $1.08 \pm 0.63mm$ is the lowest. The differences between the RMSE results for $400mm$ compared with each of the other separations were assessed using a two-sample student t-test. The difference was found to be significant at a 90% confidence interval when compared with the separation of $600mm$. The difference when compared with each of the remaining separations was significant at a 95% confidence interval. However, when compare with the separation of $250mm$ the difference was not significant.

The graph below illustrates a trend in the RMSE results, where the accuracy increases with the increase in separation towards $400mm$ and decreases at higher separations. For this reason a separation of $400mm$ between the cameras was used. This distance represents the distance between the centres of each camera; and was used in the design of the enclosure.

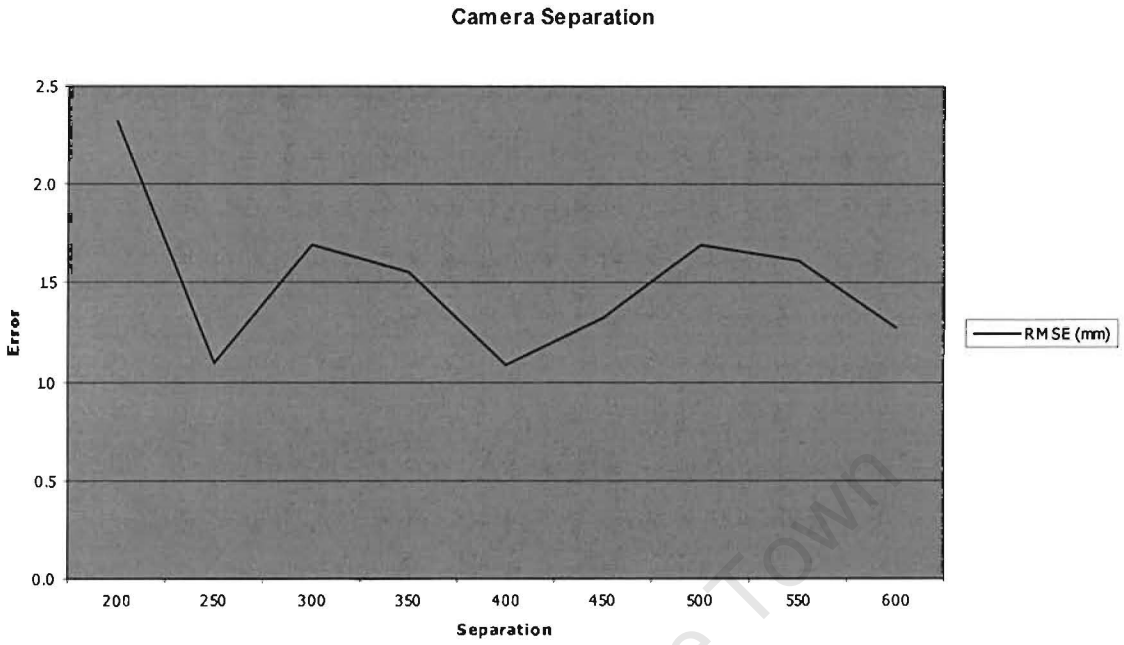

Figure 5.6 Graph of the RMSE for each camera separation

5.3 The Control Frame and Probe

The control frame (figure 5.76) comprises a grid of 6mm steel bars enclosing a volume of $200 \times 250 \times 150mm$ with 12 flattened circular plates attached to it at various points. Each plate contains a circular infrared reflective marker. The coordinates of the centres of each marker have been measured to an accuracy of $\pm 0.04mm$ in each axis, allowing the frame to be used for calibration of the operating space. The marker centres were measured using the photogrammetric system in the Department of Geomatics, UCT. The system makes use of a single Kodak DCS330 digital camera with resolution $2024 \times 1512 pixels$. The frame was positioned at the centre of a grid containing 60 reflective markers. 16 images of the grid were taken from varying positions. The 3D coordinates of the markers were found by applying a bundle adjustment algorithm using a program called Australis.

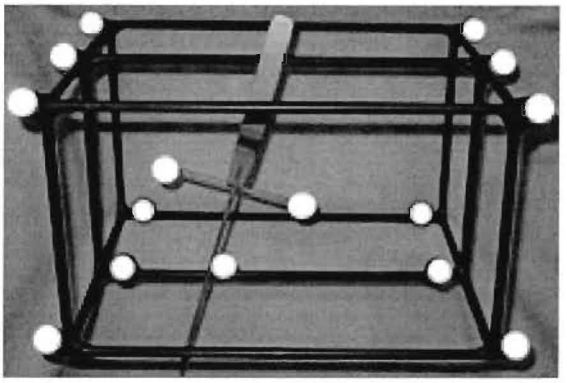

Figure 5.7 The Control Frame and Probe

The frame is used at the start of the surgical procedure to calibrate the operating space above the patient's head. This is done in order to solve the parameters of the DLT equations (described in chapter 2), which are used to transform the 2D image space of the photos into 3D physical space.

The frame is held in position, resting lightly on the patient's head, while it is photographed simultaneously on each of the smart cameras. The cameras are triggered by a mouse-click on the menu option *Calibrate Cameras* in the user interface (see chapter 6). Once the images have been taken and the space calibrated, the frame is removed. The frame is held rather than clamped to the bed, to avoid any unnecessary risk to the patient. The original design of the frame included two uprights that could be clamped in position on either side of the headrest, as shown in figure 5.8 below. The uprights were omitted from the final design due to the risk of injury to the patient while being positioned above the patient's head. The stereo pair of images of the frame is taken instantaneously and is only required once at the start of the surgical procedure, so that movement introduced by holding the frame is negligible.

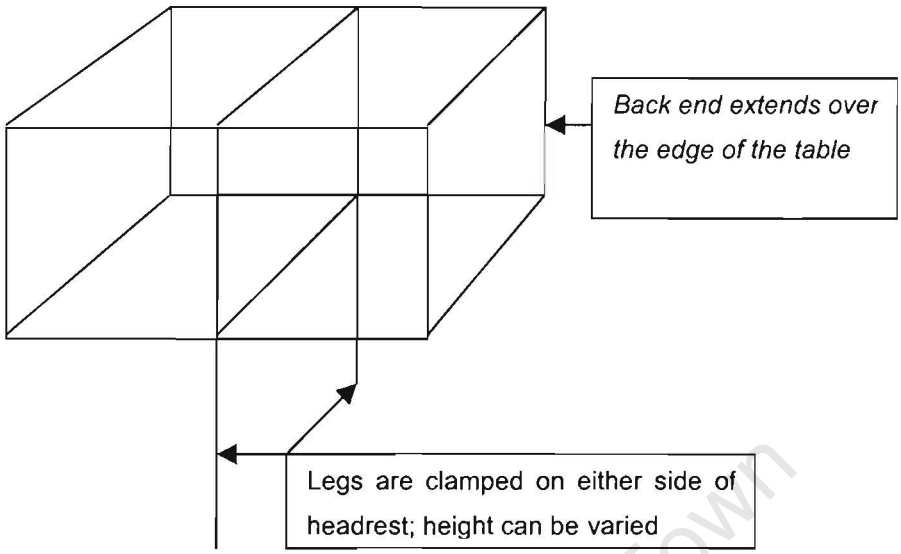

Figure 5.8 Line drawing of the original calibration frame design, excluding the marker positions

The frame was designed to enclose the volume above the patient's head in which the markers on the probe would move. The maximum possible distance of the top two markers on the pointer from the top of the patient's head determined the height of the frame. The front half of the frame rests over the surgical area containing the lesion. The back half projects over the edge of the surgical table. This arrangement includes the volume in which the markers on the probe move when the probe is held at an angle to the patient's head.

The markers were positioned around the outside of the frame so as to cover as much of the enclosed volume as possible. The four markers positioned on the back two rows at the bottom were, however, hidden from the cameras by the vertical supports. To overcome this problem the plates were moved inside the volume as shown in figure 5.7.

The frame was built and modified by Harry Hall (Department of Physiology, UCT). It was painted black to avoid interference with the marker detection from reflections off the steel bars.

The probe (figure 5.9) contains 3 circular infrared reflective markers arranged in a cross. This configuration allows for a more accurate extrapolation of the coordinates of the tip of the probe. The centre of each marker and the tip of the probe have been measured using the Reflex Microscope (Scott, 1981) to an accuracy of $10\mu m$ in the x- and y-axes and $20\mu m$ to $30\mu m$ in the z-axis. The probe is sterilised in an autoclave prior to the operation. During the operation the tip is placed at a point of interest in the surgical space within the brain, leaving the 3 markers visible to the cameras. The coordinates of the 3 markers are used to compute the coordinates of the tip using the Rodrigues transformation (Thompson, 1969) (described in chapter 2).

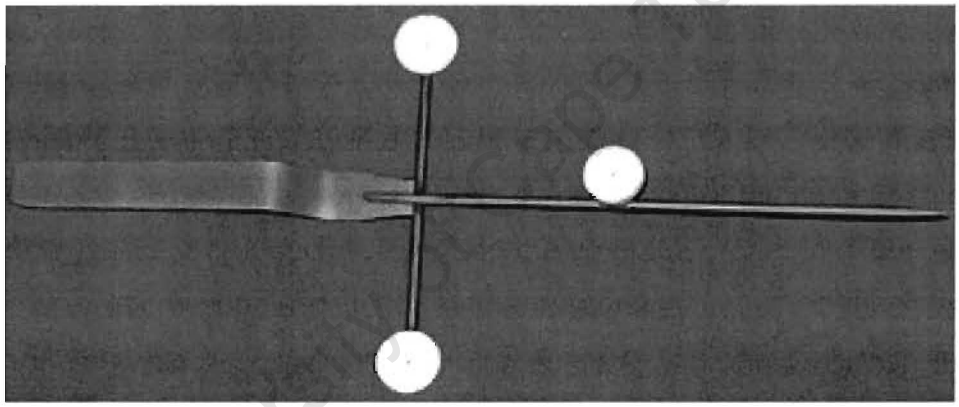

Figure 5.9 The Probe

The three markers on the probe move around in the space above the patient's head, i.e. the volume calibrated by the frame. If the probe is held in a position where the markers fall outside of this calibrated space, less accurate results will be achieved. The surgeon will need to be aware of the space in which the markers should be positioned.

CHAPTER 6

Software Development For The Photogrammetric System

The software developed for the photogrammetric system comprises two components: The software running on the laptop or computer and the software running on the cameras. The software interface on the laptop acts as a server to the two cameras. This chapter describes the communication between the laptop as server and the smart cameras as clients.

An explanation of a typical surgical operation employing the photogrammetric system is provided to present a reference base for the description of the functionality of the software interface in section 6.2.

6.1 Surgical Procedure

The procedure for a neurosurgical operation involving the removal of a tumour or lesion starts with the scanning of the lesion using either CT or MRI scanning. Four or five adhesive fiducial markers are fixed to the patient's scalp around the area containing the lesion prior to scanning to obtain good coverage of the area of interest. These fiducials have a ball bearing at their centre in the case of CT, or a dilute copper sulphate solution for MRI. The lesion is then scanned; approximately twelve slices are taken, as well as a slice through each of the fiducial markers. The order in which the fiducial markers are scanned is important for patient registration that occurs later in the procedure. Dicom images are loaded onto the laptop, either via the network or from CD. Once on the laptop, the lesion is outlined and fiducial points on the images are marked using locally developed MRIPoint software. This process is performed manually and in consultation with the neurosurgeon. The images are then compiled to produce a 3D representation

of the scanned portion of the patient's head. The CT coordinates of the lesion and fiducials are stored in text files on the laptop.

The patient is now moved to theatre and anaesthetised; the cameras are positioned above the surgical table and connected to the laptop via an Ethernet connection. The control frame is positioned above the head of the patient and a pair of images is taken to calibrate the operating space.

Patient registration entails measuring and recording the coordinates in turn of each of the fiducial markers in theatre space using the two cameras. During registration the tip of the probe is alternately positioned on the centre of each fiducial with the three reflective markers angled towards the cameras. At each position, the cameras are triggered to capture a pair of images and compute the coordinates of the markers. These are transformed to find the tip coordinates that represent the coordinates of the fiducial. Once all the fiducials have been measured the transformation parameters between physical and CT space are computed. Prior to registration the patient's head is clamped in a Mayfield clamp. After registration the fiducials are removed. The head is now covered in sterile drapes. The neurosurgeon performs the craniotomy. It is critical that nothing is disturbed during this stage of the procedure.

After the craniotomy three burr holes are drilled in the patient's skull and measured using the procedure previously described. The theatre and CT space coordinates of these three points are saved to files and thus allowing for re-registration of the system if the patient subsequently moves or the cameras are bumped. Measurements of the position of the tip of the probe can now be performed as and when required by the surgeon. The position of the tip is displayed on the nearest CT slice or can be viewed using the 3D image that was reconstructed from the CT scans

6.2 Graphical User Interface

The graphical user interface (GUI) was developed in such a way that the user is guided in a logical way through the various stages of the procedure. The GUI called Siigns (Stereo-photogrammetric Interactive Image-Guided Neurosurgical System) is illustrated in figure 6.1. The software modules accessed through the interface can be divided into 3 phases in accordance with the surgical procedure. These phases are: Image acquisition and manipulation, camera set-up and patient registration, and position measurements. The initial phase can be performed prior to the operation; the second phase is performed once the patient is in theatre but prior to the craniotomy. The final phase occurs once the craniotomy has been performed.

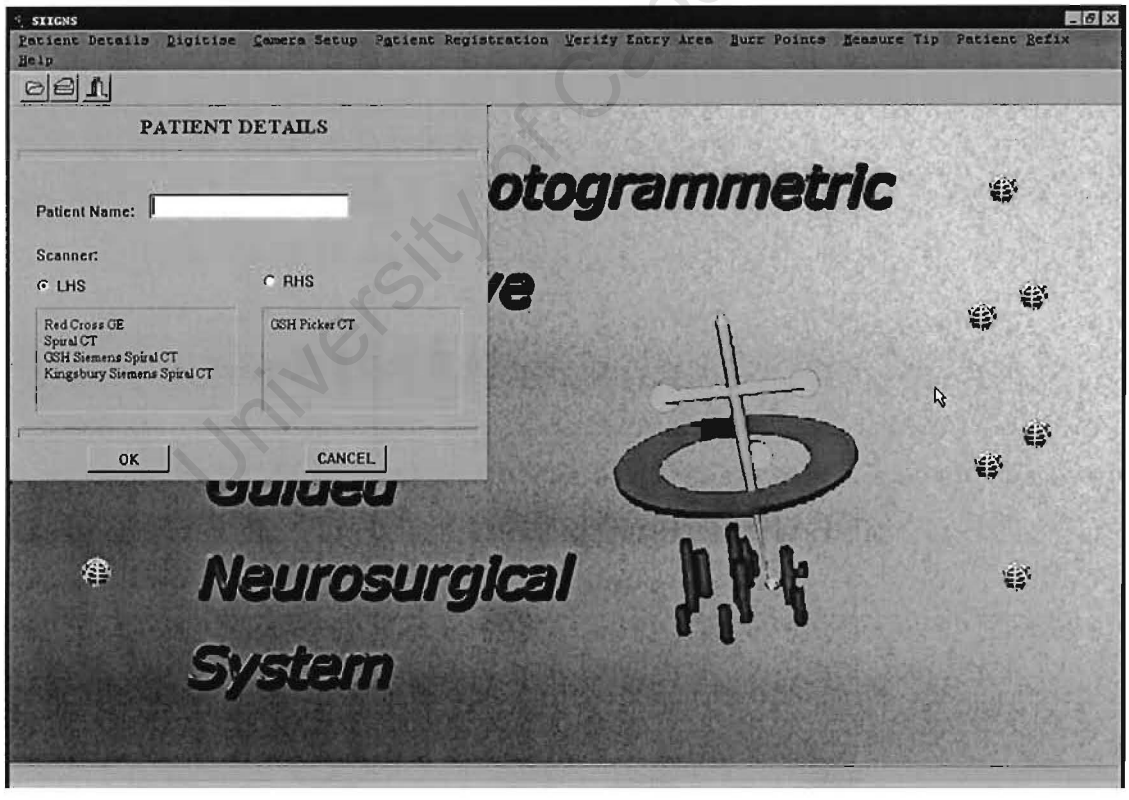

Figure 6.1 Stereo-photogrammetric Interactive Image-Guided Neurosurgical System (SIIGNS) application graphical user interface displaying the patient details box

The three phases are explained in detail in the following sections.

6.2.1 Image Acquisition and Manipulation

Before starting, the patient's name is entered as shown in figure 6.1. The first four letters are used as the patient identifier to identify files that are created during the procedure and that contain information specific to the patient. The files are labelled with the patient identifier followed by the descriptor; for example, the file holding the CT coordinates of the fiducials for the phantom is called phanct.txt, where *phan* is the patient identifier and *ct* is the descriptor for the CT coordinates of the fiducials. The choice of LHS (Left-Handed Scanner) or RHS (Right-Handed Scanner) refers to the coordinate system of the scanner. This is important when transforming coordinates from theatre space to CT space, since theatre space is determined as a right-handed coordinate system. A scanner with a left-handed coordinate system requires the y-value of the CT coordinates of the fiducials to be negated in order to solve transformations correctly. This step is performed during digitising. The patient identifier and handedness of the CT scanner are stored in a file called tempname.txt.

The second menu item is "*Digitise*" (figure 6.1) and contains two options: *Open CT Images* and *Open 3D Viewer*. Selecting *Open CT Images* calls the program MRIPointWin shown in figure 6.2. MRIPointWin is a Dicom format image viewer that was written using freeware software from MRIcro (http://www.psychology.nottingham.ac.uk/staff/cr1/mricro.html). It was designed specifically for use with the Siigns program replacing the previously used Osiris 32 (http://www.osiris.gov.au) Dicom image viewer. The viewer was replaced due to the update of the Dicom image format, which Osiris 32 could not read.

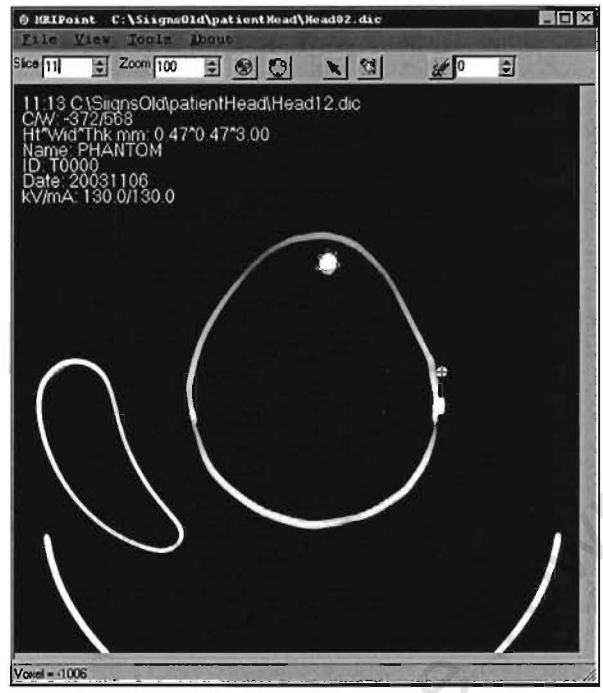

(a)

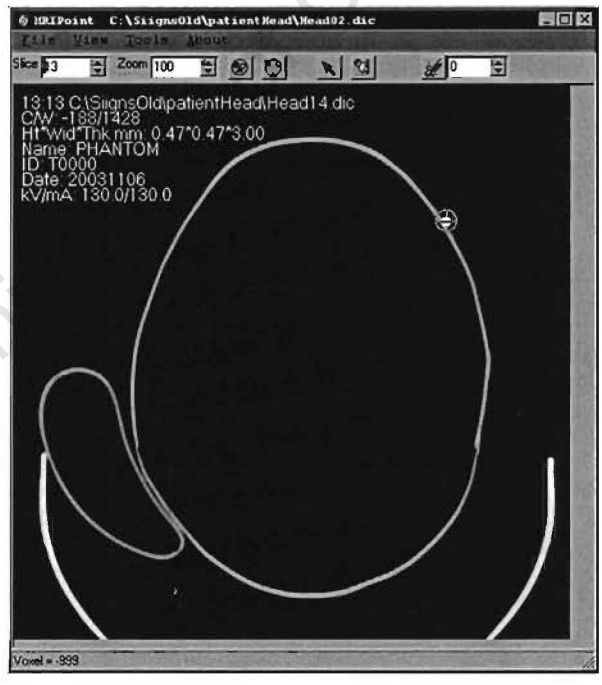

(b)

Figure 6.2 The two images show the MRIPointWin user interface displaying a CT scan taken of the head phantom. (a) shows a ROI drawn around the lesion and a cross on one of the fiducial markers. Usually these are marked on separate images. (b) displays the cross representing the tip of the probe.

The CT images are converted to Dicom format before being downloaded onto the laptop. They can then be viewed using MRIPointWin. On each image containing the lesion a region of interest (ROI) is drawn by selecting the options "*Tools* ", "*Add ROI*" from the menu and manually outlining the lesion with the mouse (figure 6.2(a)). The last few images in the series, usually four, are the scans taken through each of the fiducial markers. The fiducial on each of these is marked with a cross using the "*Add Marker*" tool in "*Tools*". The fiducials often appear on more than one image and must only be marked once in view of the fact that every marked position is counted as a separate fiducial. The coordinate system of the scanner is established and the y-value of the fiducial and ROI coordinates adjusted accordingly. The coordinates of the ROI's and fiducial markers are saved into three files: namect.txt contains the CT coordinates of the fiducials, where name is replaced by the patient identifier, nametp.txt contains the CT coordinates of the ROI and namesz.txt contains the image slice number and its associated table position (z-coordinate). These files are used in later modules of the Siigns program.

Once the lesion and fiducial coordinates have been saved the CT scans are used to reconstruct a 3D image of the scanned portion of the patients head. The 3D image shows the outline of the head containing a solid black lump representing the lesion (figure 6.3). This view can be changed to display the CT scan at the level of the tip as shown in the right image in figure 6.3. The positions of the fiducials may be viewed in this format. The image may be viewed from different angles by rotating the image.

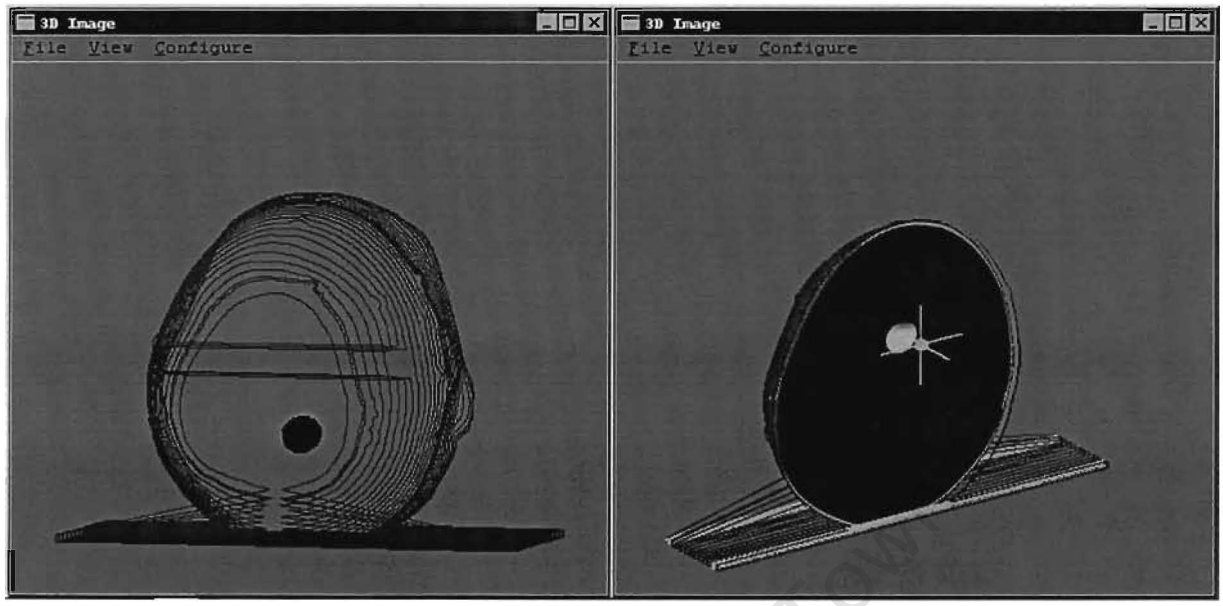

Figure 6.3. Image of the 3D Viewer displaying the 3D reconstruction of the phantom head. The left image displays the outline of the head with a solid black lump representing the lesion. The right image displays the CT scan information at the tip of the probe, displayed as a green cross.

The 3D image is kept open throughout the operation; a green cross representing the tip of the probe is displayed and its position updated whenever a measurement is performed using the *Measure Tip* module. This allows the surgeon to view where he is in 3D space. This software will be updated to display not only the current tip position, but previous positions as well to map the trajectory of the surgeon's probe.

6.2.2 Camera Set-up and Patient Registration

The second phase involves the set-up of the cameras in theatre. The patient is placed on the operating table and anaesthetised; the cameras are then clamped in place above the table and focused. The menu item *Camera Setup* (figure. 6.1) is used for the set-up and calibration of the cameras. It contains 2 options: *Focus Cameras* and *Calibrate Cameras*. These options can only be used if the cameras are switched on and the

"client" program has been executed on each of them. The GUI requires the Ethernet connection to be open before it can download images or text files from the cameras to the laptop. If the "client" program is not operating on both cameras an error will be displayed and the GUI will close.

The menu option *Focus Cameras* opens the window illustrated in figure 6.4(a), for each camera. Images may be downloaded off the cameras and viewed in the windows. These windows must be left open during the operation since the closure of a window disconnects the link to the cameras. However, they can be hidden using the *Hide* button. The user has the option of downloading images as either a single image using *Get Image* or as a real time stream of images using *Stream*, allowing the user to manually focus each camera and set the aperture on the lens. The shutter speed can be changed in the configuration screen shown in figure 6.4(b) to best suit the lighting conditions in theatre. Selecting or deselecting the LED Flash Unit will turn the infra-red flash on or off.

(a)

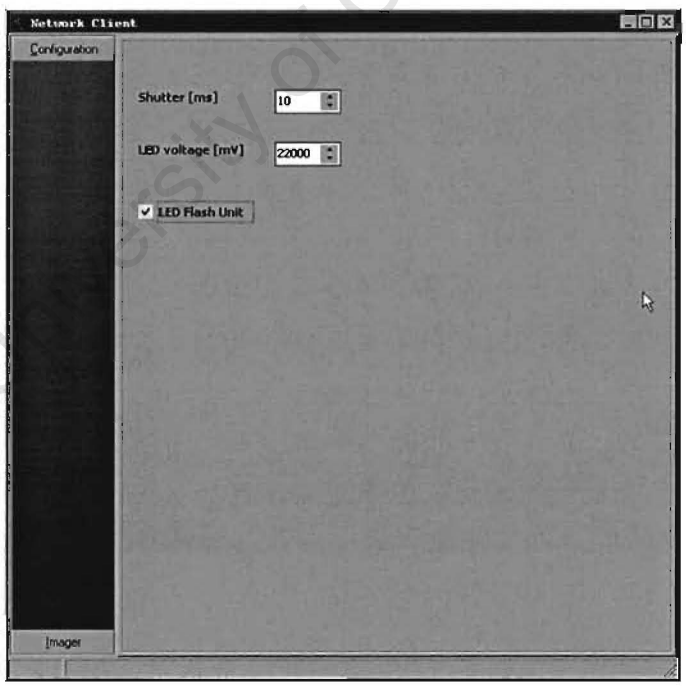

(b)

Figure 6.4 (a) Client Window showing an image of the probe downloaded off the camera. (b) The configuration screen where the shutter speed is set, the LED flash unit is turned on/off, and the LED voltage is set.

The menu option *Calibrate Cameras* connects to the cameras via the Ethernet connection triggering them to take a stereo pair of images. Each camera executes the pattern recognition algorithm described previously on the image to identify the 12 markers on the control frame. The 2D coordinates of the markers are downloaded to the laptop from each camera. The DLT (see chapter 2) is performed and the transformation parameters for transforming 2D image coordinates into 3D physical space are computed and saved to the files ParamL.txt and ParamR.txt for the left and right cameras respectively. The source code to communicate with the cameras was supplied by EDH (Stellenbosch, South Africa) along with the cameras. The code was modified for communication with the GUI. The additional functions are explained in section 6.3.1.

Patient Registration is performed once the cameras have been set up. The module reads in the number of fiducials used from the file namect.txt. The user is then instructed to position the tip of the probe at the centre of the first fiducial and to trigger the cameras by clicking on the "OK" button with the mouse to take a measurement. This is repeated for each fiducial until all the fiducials have been measured. The order in which the fiducials are measured is critical. In order to perform the transformation from physical space to CT space correctly, it is essential that the fiducials be measured in the same order as they were scanned. Every time the cameras are triggered to measure a fiducial marker each camera executes the pattern recognition algorithm to identify the coordinates of the 3 markers of the probe in the image. These 2D image coordinates are downloaded to the laptop where they are transformed into 3D physical coordinates using the transformation parameters from the DLT. Using the accurately known 3D coordinates of the 3 markers and tip of the probe as determined using the Reflex Microscope (Scott, 1981), the Rodrigues transformation (Thompson, 1969) described in chapter 2, is performed to find the coordinates of the tip of the probe. In this way the physical coordinates of all the fiducial markers are measured. Once all the fiducials have been measured and their 3D physical space coordinates recorded in the file nametg.txt, the module opens namect.txt and extracts the coordinates of the fiducials as obtained from the CT scans. The Rodrigues transformation is performed to

find the parameters to transform measured 3D coordinates into CT scan values. The parameters are saved in a file called namebbp.txt.

The RMSE between the measured coordinates of the markers on the probe and the calibrated coordinates is computed for each fiducial to determine whether the accuracy of the measurement is acceptable or whether it should be repeated. The measurement is considered satisfactory if the RMSE is below $0.7mm$ and the maximum error in each axis is less than $1.2mm$. The errors of the transformation are displayed on screen with a dialog box informing the user whether to continue or repeat the measurement. The option to re-measure a fiducial is provided with each measurement.

The next module, *Verify Entry Area* (figure 6.1) is used to measure and display the entry area in order to verify the positions of critical structures. The module requests the user to select three of the fiducials for use as burr points. The probe is positioned at the planned entry point. The module then measures the position of the probe and opens a viewer displaying the CT slice nearest the measured point. The slice contains a cross where the tip of the probe is positioned (figure 6.2(b)).

The surgeon can also use this option as a means of verifying the accuracy of the patient registration.

6.2.3 Position Measurements

The *Burr Point* module is employed once the craniotomy has been performed. The surgeon drills 3 small holes into the patient's skull around the removed portion of skull. The three burr holes are then measured and the 3D coordinates stored in a file called namebp.txt. The 3D coordinates are transformed into CT values and stored in a file called namebg.txt. If motion should subsequently occur, these burr holes can be re-measured and used to compute new transformation parameters from physical space to CT slice values.

The module *Measure Tip* is used to take measurements during the operation. There are two options: *Measure* and *Manual Recognition*. Whenever *Measure* is selected, the cameras are triggered to take a pair of images and to identify the 2D coordinates of the markers on the probe on the left and right images, respectively. These are downloaded to the laptop where the DLT and Rodrigues transformations are computed to find firstly the 3D physical space coordinates of the tip of the probe as explained previously. Using the transformation parameters that were computed during Patient Registration, the 3D physical coordinates of the tip are transformed to CT coordinates. These coordinates are then passed to the 3D viewer, which displays a green cross on the 3D image that represents the position of the tip of the probe as shown in figure 6.3. The coordinates are also displayed as a cross in a circle on the nearest CT slice as shown in figure 6.5. This gives the surgeon both a 2D and a 3D view of the probe's location within the patient's brain.

The second option, *Manual Recognition*, opens a screen, described in section 6.2.4, where the user can manually select the markers when the recognition program produces large errors due to extraneous light and reflections.

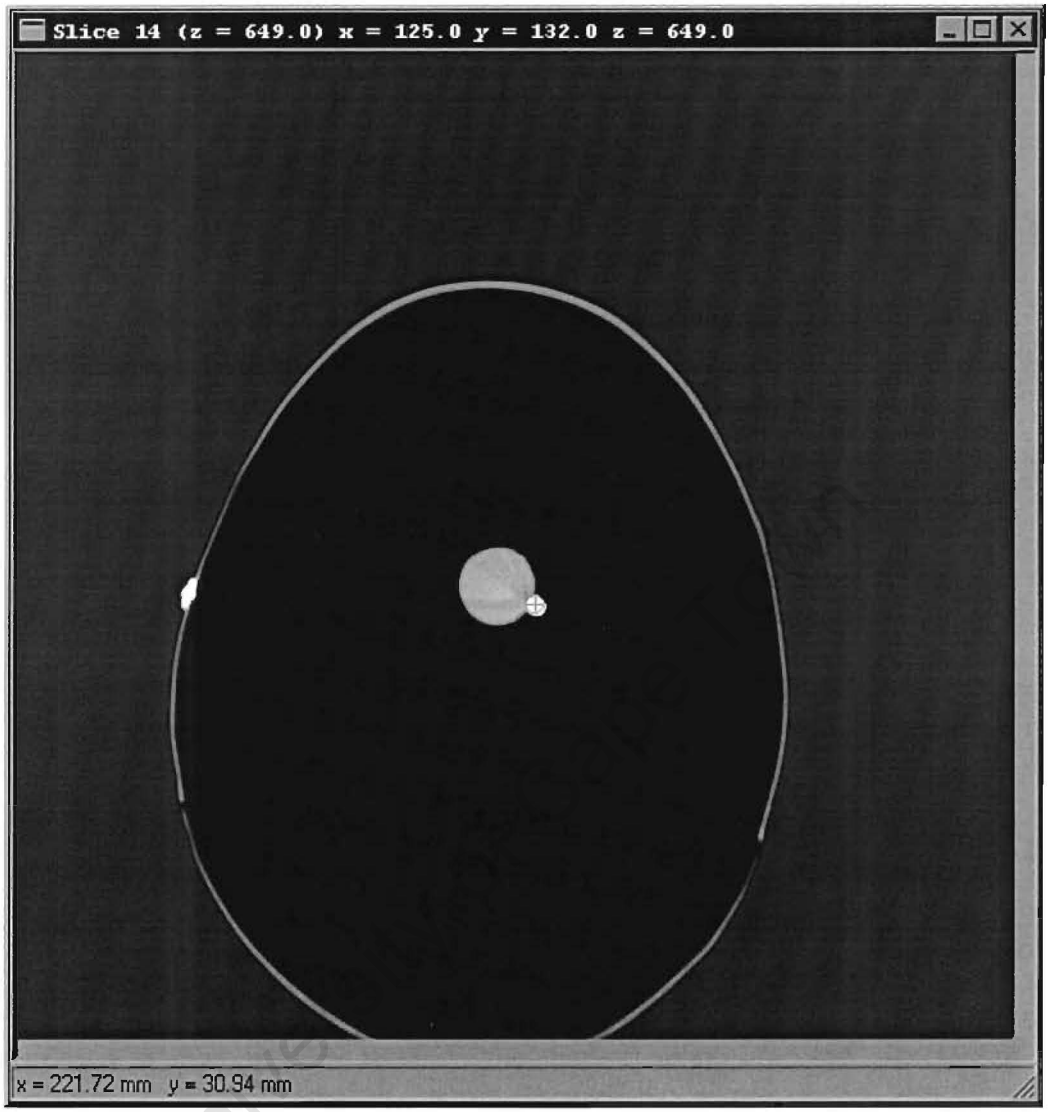

Figure 6.5 A 2D CT slice displaying a blue cross in a circle representing the tip of the probe. The CT coordinates of the tip are displayed in the title bar.

The final module *Patient Refix* is only used if the patient moves relative to the cameras. When this happens the patient registration performed earlier becomes invalid. The patient identifier is entered and the patient is re-registered using the Burr holes that were drilled during the craniotomy. The procedure followed in Patient Registration is repeated.

6.2.4 Manual Recognition Module

The Manual Recognition module (fig. 6.6) is used when the recognition program on the cameras is unable to detect the markers due to spurious reflections or partial obstruction of a marker.

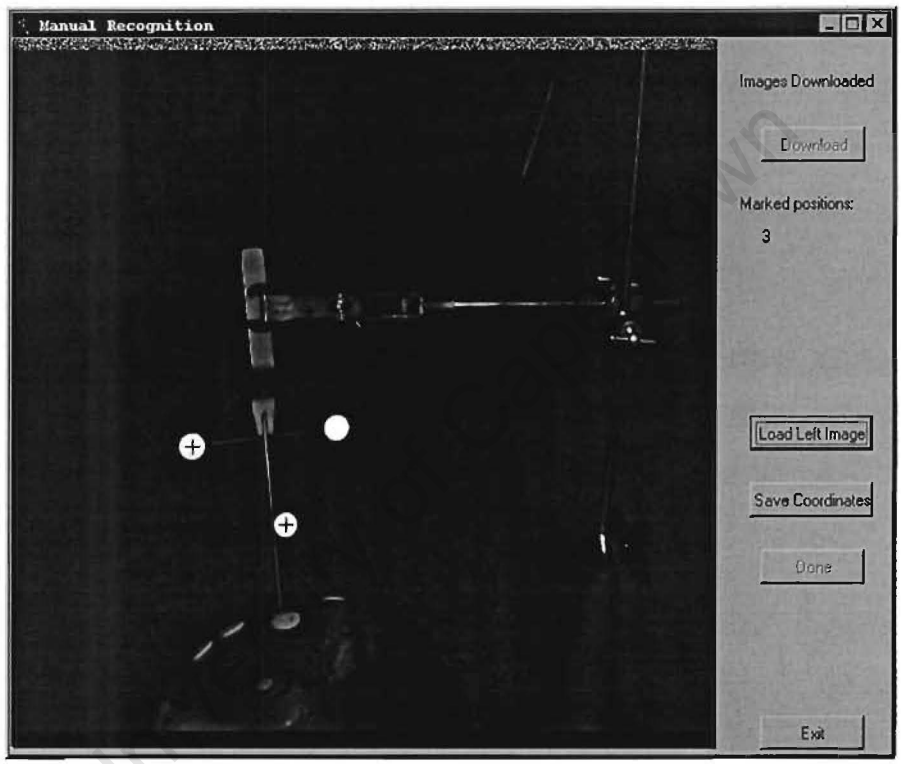

Figure 6.6 The Manual Recognition Interface for manually selecting markers when the recognition program fails. The red crosses show selected markers.

The user uses the button *Download* to trigger the cameras to take a pair of images and download them onto the laptop. The user then opens the left image and manually selects the markers by positioning a red cross over each marker and clicking on it using the mouse. The coordinates are saved and the process repeated for the right image.

The user then clicks the button *Done* to indicate that all the markers have been selected.

The module obtains the 2D coordinates by finding the centre of gravity of each selected marker (see chapter 2) for the left and right images. The coordinates are then passed to the main program. The module can be used during patient registration, position measurements or camera calibration. The program continues with the current process accepting the coordinates as if they were downloaded from the cameras.

6.3 Client-Server Communication with the Smart Cameras

The cameras act as clients to the Siigns application software running as a server on the laptop. Each camera runs a client program: *clientl* on the left camera, *clientr* on the right camera. The client program receives messages from the laptop and carries them out; either downloading an image or text file to the laptop, or to change a setting on the camera, such as the shutter speed.

The first prototype smart camera provided by EDH did not have the client software loaded onto it. This had to be performed every time the camera was switched on. HyperTerminal allowed the user to connect to the camera via the serial port. It was used to download the client program and change its permissions in order to run it. A script was then downloaded to provide the camera with an IP address and run the client program to connect to the computer via the Ethernet. The sensor software provided by EDH also had to be downloaded onto the camera at start-up. The HyperTerminal connection was made via the serial port at 9600 Baud, 8 data bits and 1 parity with no flow control. This could then be increased to 115200 Baud.

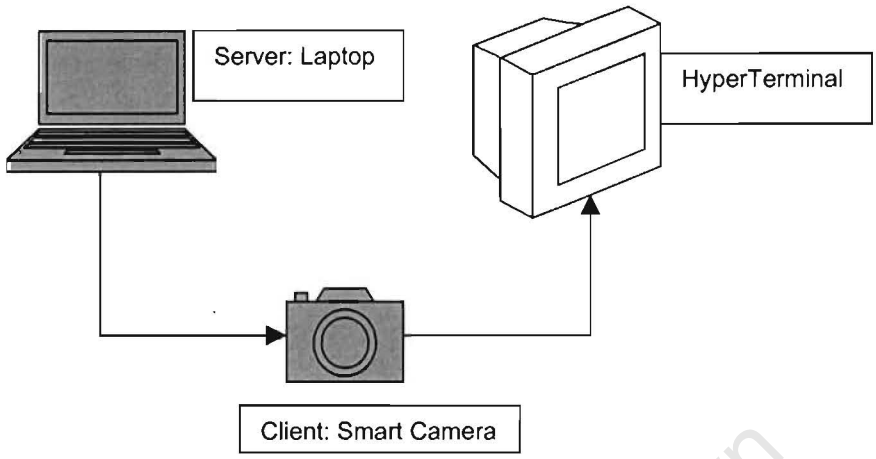

Figure. 6.7 Diagram of the Server Client set-up

The new cameras have the sensor software in permanent memory and the IP address saved into flash memory. The client software will be saved into flash memory once it is complete. Download onto the camera is now achieved by using file transfer protocol (ftp) to transfer the file to the cameras across an Ethernet link. Telnet is used to access the cameras via the Ethernet link.

6.3.1 Linux Compilation

Each smart camera runs a modified version of the Debian Linux operating system (Refer to Ch. 5.3.1). This is a streamlined version that does not include a C/C++ compiler, so that the programs written for the camera need to be pre-compiled. They are compiled on a computer operating on Debian Linux, version 2.4.16. A Debian Linux cross-compiler, version 2.4.18, has been installed. The cross-compiler is used to compile programs to run on the smart cameras.

The three main functions of the client program running on the camera, which communicate with the Siigns Interface Application on the laptop, are

- GetImage: Takes an image and downloads it to the laptop.
- Calibrate: Takes an image, runs the pattern recognition algorithm on the image and downloads a text file containing the 2D coordinates of the 12 markers of the control frame.
- Measure: Takes an image, runs the pattern recognition algorithm on the image and downloads a text file containing the 2D coordinates of the 3 markers on the probe.

Further functions include changing the shutter speed and adjusting the LED flash unit.

Each camera has a slightly different version of the client program, in order to distinguish between the files being downloaded onto the laptop. The left camera downloads an image called t1.ppm; the right image is called t2.ppm. The left camera downloads a text file called CamL.txt; the right text file is called CamR.txt.

CHAPTER 7

Photogrammetric System Testing

The Stereoscopic Photogrammetric Guidance System, described in the previous two chapters, underwent rigorous testing under laboratory and theatre conditions. The method and results of the investigation are presented and discussed in this chapter.

Grunert, et al. (2003) divides up the system accuracy into the technical error, the registration error and the application error. The technical error refers to the calculation of the device's position in space. The registration error is due to the transformation from physical space into image space. The application error results from anatomical brain shift during the operation.

Steinmeier, et al. (2000) uses a similar distinction between the various contributions to the system accuracy, although they define an additional area for error, namely the voxel size or distortion of the image data.

The photogrammetric system testing has been divided up into the system accuracy and repeatability, the error of recognition of the control frame and probe markers, and the registration error. The system has not yet been used in clinical trials and therefore the application error has not been included. Since the voxel size contributes to the calibration error it has not been tested separately.

7.1 Phantom Testing in the Laboratory

The following areas were investigated in the laboratory:

- The system accuracy

- The repeatability
- The calibration and recognition accuracy
- The registration accuracy

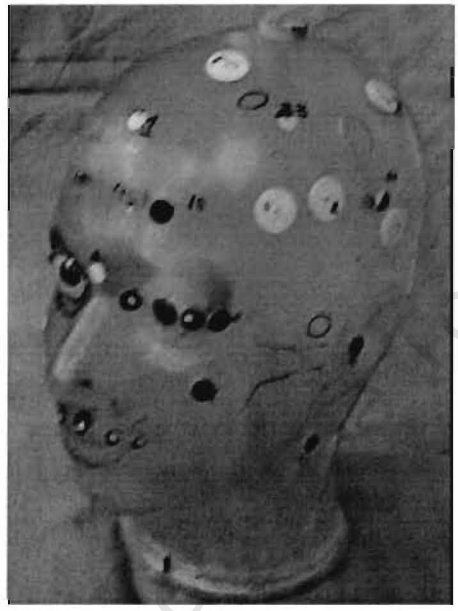

Figure 7.1 Head phantom: a perspex head containing a tumour

7.1.1 Method

Two methods were employed in the investigation. The first method followed the surgical procedure where the CT coordinates of the measured points were compared to the coordinates obtained from the CT scans. The second method followed the same procedure except the physical space coordinates of the measured points were transformed into the calibrated reference frame and compared to the more accurate calibrated coordinates.

Method one used both a head phantom (figure 7.1), a perspex model of a head containing a perspex tumour, and a rod phantom consisting of a perspex base

containing 15 columns of differing heights and positions in a 3D volume, described in chapter 4. The procedure described in the previous chapter was followed. Both phantoms were scanned using the spiral CT scanner at Groote Schuur Hospital and the images copied onto the laptop from a CD.

Four ball bearings were attached to the head phantom as fiducials. Two ball bearings were attached to the tumour as tumour points. A CT slice was taken through each of the fiducials and nine slices through the tumour. The two tumour points appeared on the scans.

The cameras were set up at a distance of 1.5m from the phantom (figure 7.2). The control frame was held in place above the phantom and the cameras calibrated. The four fiducials were measured to register physical space to CT space. They were re-measured along with the ball bearings positioned on the tumour and compared to the coordinates obtained from the CT scans. This information was used to determine the accuracy of the system. The repeatability was determined by repeatedly measuring each fiducial and repositioning the probe at varying angles between measurements.

A CT slice was taken through each of the ball bearings on the rod phantom. Four of the points were used as fiducials. The same procedure as before was followed to measure the system accuracy. Once the phantom was registered to CT space, each of the points was measured and compared to the coordinates obtained from the CT scans. The three highest columns were excluded as they were difficult to measure and therefore the accuracy would be difficult to determine and the results skewed.

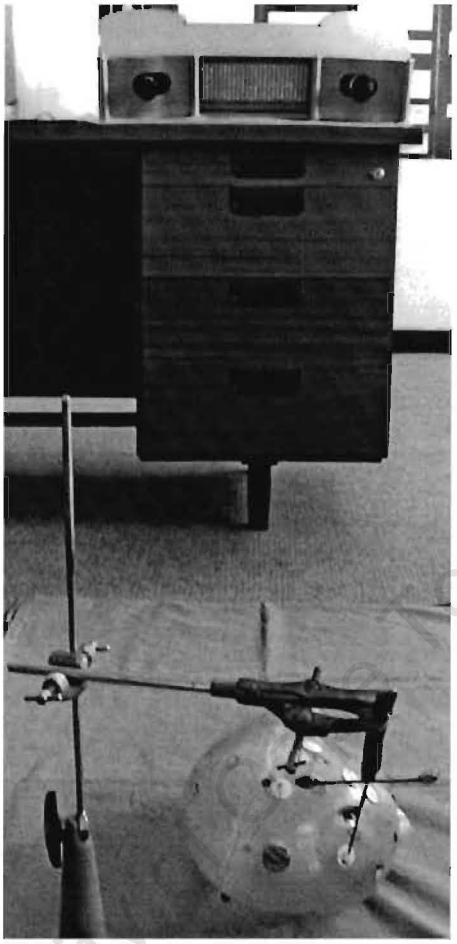

Figure 7.2 Laboratory set up of cameras

In method two the theatre values of the measurements obtained using the rod phantom were compared to the accurately known coordinates measured using the Reflex Microscope (Scott, 1981) (see chapter 2). These results were then compared to the results obtained using the rod phantom in method one to determine the error introduced by the transformation into CT space.

The registration accuracy was investigated by repeating the registration several times using four fiducials. The registration process transforms the measured physical coordinates of the fiducials into CT coordinates. The accuracy of the transformation was used as the registration accuracy.

The recognition and calibration accuracy were investigated by comparing the measured 3D coordinates to the accurately known coordinates of the three markers on the probe and the twelve markers on the frame, respectively (see chapter 5).

The results from both methods are presented below.

7.1.2 Results

7.1.2.1 Accuracy

The accuracy of the system was assessed from measurements of the fiducial and tumour points on the head phantom using the first method described above. The results are presented in table 7.1. The errors obtained from measurements of the rod phantom are presented in tables 7.2 and 7.3, using the first and second methods, respectively.

The root mean square error was computed for each measurement. The mean, standard deviation and maximum value of the error in the x-, y- and z-axes and the RMSE were found for the fiducial and the tumour points. The combined mean and standard deviation were found for all the points measured.

Table 7.1 Errors obtained with the Stereo-photogrammetric navigation system using the head phantom. The normal surgical procedure was followed (method one). The combined mean refers to all the points measured.

		Δx (mm)	Δy (mm)	Δz (mm)	RMSE (mm)
Fiducials	Mean	0.7	0.6	1.3	1.8
	Std Dev	0.6	0.4	1.0	1.0
	Max	4.1	2.2	4.5	6.1
Tumour	Mean	1.7	1.1	1.3	2.7
	Std Dev	1.1	0.8	0.7	0.9
	Max	4.6	3.1	3.0	5.3
Combined	Mean	0.9	0.7	1.3	2.0
	Std Dev	0.8	0.6	1.0	1.1
	Max	4.6	3.1	4.5	6.1

Table 7.2 Errors obtained with the Stereo-photogrammetric navigation system accuracy using the rod phantom. The normal procedure for a surgical operation was followed (method one).

	Δx (mm)	Δy (mm)	Δz (mm)	RMSE (mm)
Mean	0.7	1.1	1.8	2.6
Std Dev	0.6	1.1	1.0	1.1
Max	2.8	4.6	4.5	6.2

Table 7.3 Errors obtained with the Stereo-photogrammetric navigation system accuracy using the rod phantom. The physical space coordinates were compared to the known coordinates found using the Reflex Microscope (method two).

	Δx (mm)	Δy (mm)	Δz (mm)	RMSE (mm)
Mean	0.8	0.7	1.5	2.0
Std Dev	0.6	0.6	0.9	0.8
Max	3.2	3.4	3.6	4.3

In method one the accuracy was investigated using the head phantom containing four fiducial markers and two tumour points. The mean and standard deviation of the errors are found to be $0.9 \pm 0.8mm$ in the x-axis, $0.7 \pm 0.6mm$ in the y-axis and $1.3 \pm 1.0mm$ in the z-axis. The mean and standard deviation of the RMSE are found to be $2.0 \pm 1.1mm$ with an absolute maximum difference of $6.1mm$. The mean RMSE of the fiducials is $1.8 \pm 1.0mm$. The mean RMSE of the points on the tumour is higher at $2.7 \pm 0.9mm$. This was expected since the tumour points are deeper and not part of the registration process.

The rod phantom consisting of 15 points, whose coordinates are accurately known, was measured using method one. The RMSE is found to be $2.6 \pm 1.1mm$ with an absolute maximum distance of $6.2mm$. The comparison of the physical space coordinates of the measurements to the accurately known coordinates, in method two, determined the mean and standard deviation of the RMSE to be $2.0 \pm 0.8mm$ with an absolute maximum distance of $4.3mm$. This was expected since the Reflex Microscope is of a greater accuracy than CT.

7.1.2.2 Repeatability

The repeatability of the system was ascertained by repeatedly measuring a number of points on each phantom. The results are presented in table 7.4.

The absolute differences between measurements of a specific point were found and the mean and standard deviation of these differences computed. In addition, the root mean square error was computed for each repetition and the absolute difference between these determined. The mean and standard deviation of the RMSE's were computed.

Table 7.4 Repeatability of the Stereo-photogrammetric navigation system using both the head and rod phantoms. The repeatability was measured by repeatedly measuring the same point while varying the angle of the markers on the probe to the cameras.

	Δx (mm)	Δy (mm)	Δz (mm)	RMSE (mm)
Mean	0.7	0.7	1.4	1.9
Std Dev	0.6	0.6	1.1	1.1
Max	2.8	2.9	4.0	4.7

The mean and standard deviation of the RMSE are found to be $1.9 \pm 1.1mm$ while the absolute maximum difference between two measurements of the same point is $4.7mm$.

For the head phantom the repeatability is $1.8 \pm 1.0mm$, compared to $2.5 \pm 1.0mm$ for the rod phantom.

7.1.2.3 Calibration and Recognition Accuracy

The accuracy of the recognition algorithm was determined using the physical space coordinates produced by the DLT over several trials. The results represent the error between the measured physical space coordinates of the frame during calibration and the accurately known coordinates of the frame. The mean, standard deviation and maximum errors were found for the x-, y- and z-axes and the RMSE.

This process was repeated with both the control frame, in order to ascertain calibration accuracy (table 7.5), and the probe (table 7.6).

Table 7.5 Errors obtained during camera calibration with the Stereo-photogrammetric navigation system.

	Δx (mm)	Δy (mm)	Δz (mm)	RMSE (mm)
Mean	0.4	0.5	0.4	0.9
Std Dev	0.3	0.5	0.4	0.5
Max	1.1	1.8	1.4	2.1

Table 7.6 Errors obtained during recognition of the markers on the probe

	Δx (mm)	Δy (mm)	Δz (mm)	RMSE (mm)
Mean	0.2	0.2	0.5	0.6
Std Dev	0.1	0.2	0.3	0.3
Max	0.6	0.8	1.2	1.4

The RMS error obtained for the twelve markers on the control frame is $0.9 \pm 0.5mm$ compared with the RMS error for the three markers on the probe of $0.6 \pm 0.3mm$. The Rodrigues transformation (refer to chapter 2) was used to find the transformation parameters from physical space into the reference frame and determine the accuracy of the transformation. It shows a lower accuracy when using more points.

7.1.2.4 Registration Accuracy

The accuracy of the patient registration was determined for repeated registration of the head phantom. The mean, standard deviation and maximum errors were found in the x-, y- and z-axes. The RMSE was computed for each measurement. The results are presented in table 7.7.

Table 7.7 Errors obtained during registration.

	Δx (mm)	Δy (mm)	Δz (mm)	RMSE (mm)
Mean	0.3	0.5	0.6	0.9
Std Dev	0.2	0.3	0.5	0.4
Max	0.7	1.2	1.5	1.8

The mean and standard deviation of the RMS error of registration is determined to be $0.9 \pm 0.4mm$.

7.2 Theatre Trials

The theatre trials had two objectives: to demonstrate the system to the Neurosurgeons and to test it in theatre. The areas defined for investigation in theatre were as follows:

- The system accuracy
- System repeatability
- The effect of the operating lights on the calibration and recognition accuracy

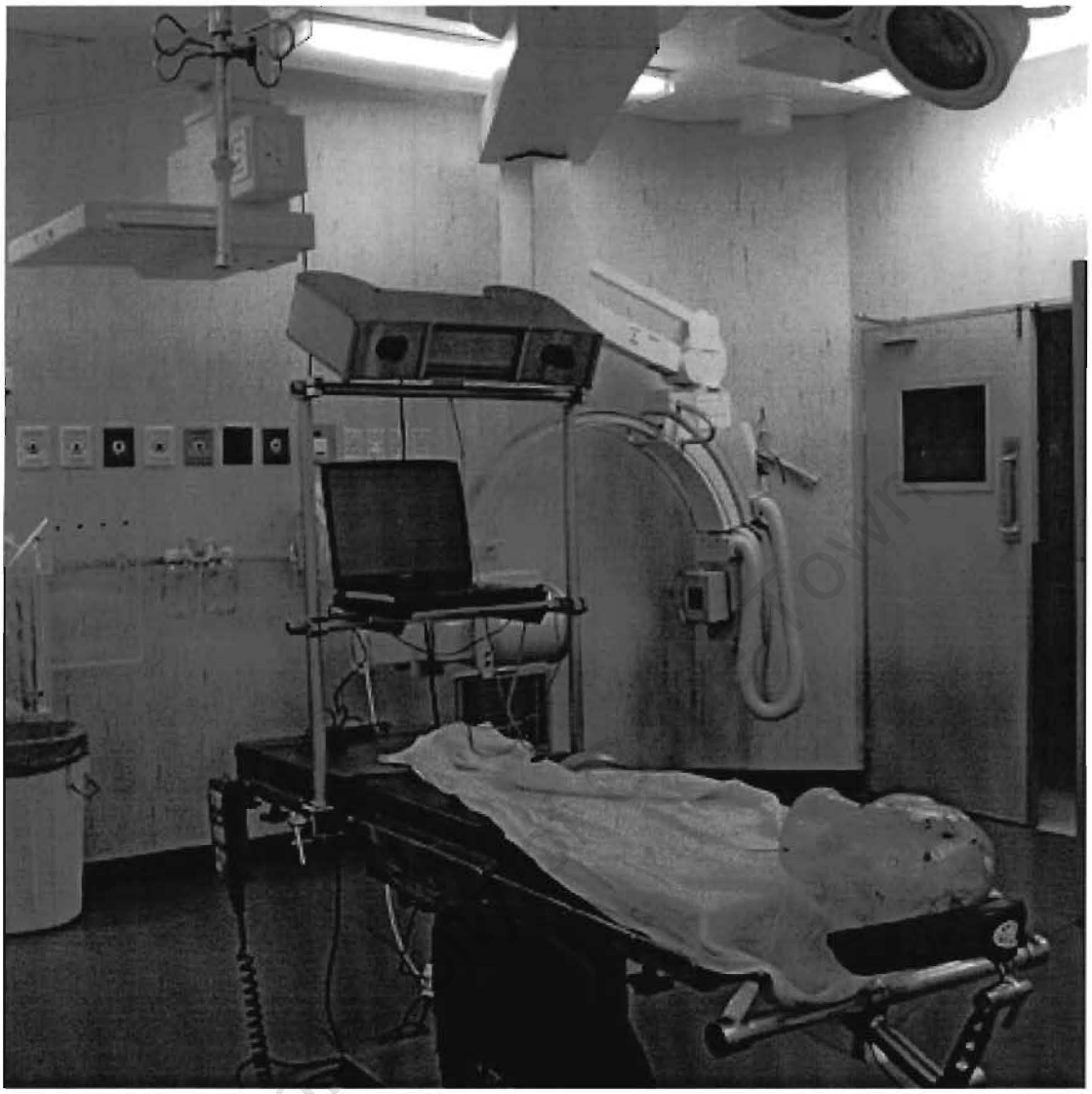

Figure 7.3 The operating table with the cameras and laptop set up.

7.2.1 Method

The method followed the standard surgical procedure and the cameras were positioned accordingly (figure 7.3). The laptop was positioned on the stand below the cameras to emulate the position of the monitor during the operation. The head phantom was used.

The phantom was placed on the horseshoe headrest with the point of entry accessible to the surgeon (figure 7.3).

Four fiducials were used to register theatre or physical space to CT space. They were then re-measured with the probe and compared to the coordinates obtained from the CT scans. This information was used to determine the accuracy of the system. Repeatedly repositioning and measuring the position of the probe at different angles on two of the fiducial markers determined the repeatability of the system.

The effect of the lights on the calibration was measured by setting the frame up in a fixed position and performing the calibration with the operating lights directed towards it, away from it and switched off. The results were compared and assessed.

The recognition accuracy was determined by comparing the measured physical space 3D coordinates of the three markers on the probe to the accurately known coordinates.

7.2.2 Results

7.2.2.1 Accuracy

The accuracy of the system was assessed from measurements of the fiducial and lesion points using the method described above. The mean and standard deviation of the errors in each axis were found. The RMSE was computed for each measurement and the mean and standard deviation found. The results are presented in table 7.8.

Table 7.8 Errors obtained with the Stereo-photogrammetric navigation system using head phantom in the theatre. The normal procedure for a surgical operation was followed.

	Δx (mm)	Δy (mm)	Δz (mm)	RMSE (mm)
Mean	0.7	0.5	1.1	1.6
Std Dev	0.6	0.5	0.7	0.8
Max	3.5	2.0	2.5	3.9

The mean and standard deviation of the RMS errors are $1.6 \pm 0.8mm$ with an absolute maximum error of $3.9mm$.

7.2.2.2 Repeatability

The repeatability of the system was ascertained by repeatedly measuring a number of points on the phantom. The results are presented in table 7.9. The absolute differences between repeated measurements of the same point were found in the x-, y- and z-axes and the mean and standard deviation of these differences computed. In addition, the RMSE was computed for each repetition and the absolute difference between these determined. The mean and standard deviation of the RMSE's were computed.

Table 7.9 Repeatability of the Stereo-photogrammetric navigation system in theatre using the head phantom. The repeatability was measured by repeatedly measuring the same point while varying the angle of the probe to the cameras.

	Δx (mm)	Δy (mm)	Δz (mm)	RMSE (mm)
Mean	2.3	1.6	2.0	3.8
Std Dev	1.5	1.0	1.3	1.4
Max	4.7	3.6	5.0	6.0

The mean and standard deviation of the RMSE of the absolute difference between repeated measurements of the same point are $3.8 \pm 1.4mm$ while the maximum difference between two measurements of the same point is $6.0mm$.

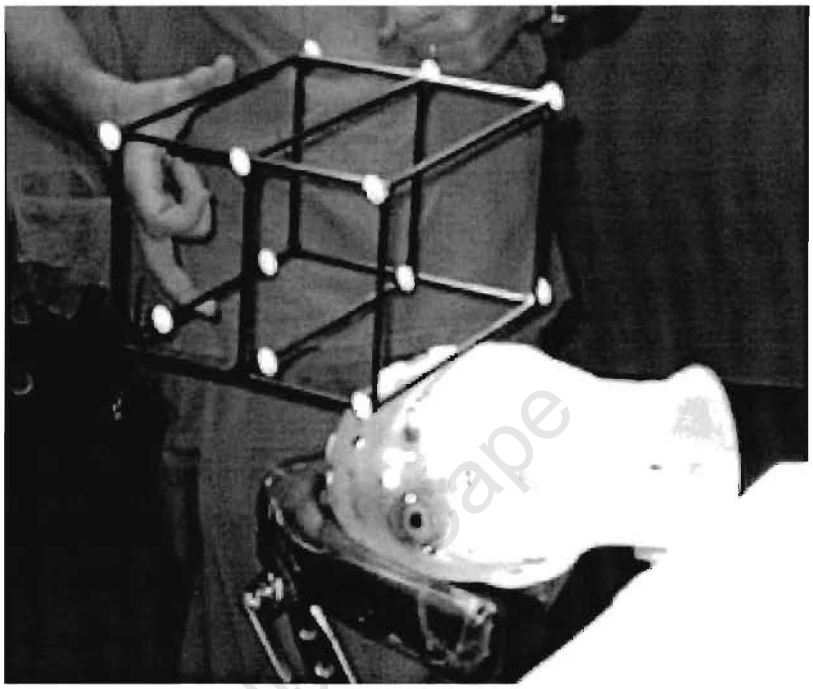

Figure 7.4 Illustration of the reflections generated by the operating lights

7.2.2.3 The effect of the operating lights on the Calibration

The operating lights are intense and as a result cause reflections off most items in the theatre as shown in figure 7.4. The cameras pick up spurious reflections off these items including the surgical drapes. The effect of the lights on the accuracy of the camera calibration was investigated using the results produced by the DLT over several trials. The calibration was performed with the operating lights directed towards the frame, away from the frame and switched off. The results are presented in table 7.10. These results represent the error between the measured coordinates of the frame after

calibration and the accurately known coordinates of the frame. The mean, standard deviation and maximum errors were found for the x-, y- and z-axes.

Table 7.10 The effect of the operating lights on the calibration. The lights were directed towards the frame, away from the frame and switched off.

	Δx (mm)		Δy (mm)		Δz (mm)	
Position of lights	Mean	Std Dev	Mean	Std Dev	Mean	Std Dev
Towards Frame	0.5	0.8	0.5	1.4	0.9	1.7
Away from Frame	0.4	0.8	0.6	1.2	0.5	1.0
Off	0.4	0.7	0.5	1.1	0.5	1.0

The results in table 7.10 are very similar, differing mainly in the z-axis. The errors in the z-axis were greatest when the lights were directed at the frame. For the lights directed away and off the errors were improved and similar.

7.2.2.4 Recognition Accuracy

The recognition accuracy was determined by comparing the measured 3D coordinates in physical space of the markers on the probe to the calibrated coordinates. The mean, standard deviation and maximum errors were found for the x-, y- and z-axes and the RMSE. The results are presented in table 7.11 below.

Table 7.11 Results of the investigation into the accuracy of recognition of the markers on the probe under the operating lights in theatre

	Δx (mm)	Δy (mm)	Δz (mm)	RMSE (mm)
Mean	0.2	0.1	0.5	0.6
Std Dev	0.1	0.1	0.3	0.3
Max	0.5	0.6	1.3	1.4

The mean and standard deviation of the RMSE are $0.63 \pm 0.26mm$ with an absolute maximum error of $1.38mm$. The operating lights cause reflections off the handle of the probe. These may be picked up by the cameras and determined to be markers. The resulting errors are large and therefore rejected by the program, however, this occurred roughly 10% of the time and it may be a problem during surgery.

7.3 Discussion

7.3.1 Laboratory

Method one, using the rod phantom, determined the accuracy to be $2.6 \pm 1.1mm$ with a maximum distance of $6.2mm$. These values reflect the mean and standard deviation of the RMS errors between measurements of the 3D coordinates of points on the phantom and the CT scan coordinates of the points. The accuracy is determined to be $2.0 \pm 0.8mm$ with a maximum distance of $4.3mm$ when the measured 3D coordinates in physical space are compared to the accurately known coordinates of the points (method two), measured using the Reflex Microscope (Scott, 1981). The accuracy found by comparing the measured coordinates to the CT coordinates is lower than when compared with the accurately known coordinates.

This may be due to several reasons: the measurements obtained from the CT scans measure the middle of the ball bearing although the tip rests against the top; the scans

are 2mm thick and taken through each ball bearing; where more than one appeared in a slice, only one scan was taken, therefore on some of the CT measurements the depth (z-axis) may be slightly off. The investigation shows that the accuracy of the camera system is high and errors are introduced when transforming into CT values. This error can be reduced using lower slice thickness, e.g. 1mm, when scanning. In theatre the ball bearings are removed, therefore the middle is being measured during Patient Registration and not the top as in the case of the rod phantom.

Method one, using the head phantom, determined the system accuracy to be $2.0 \pm 1.1mm$ with a maximum distance of $6.1mm$. This compares well with the $2.0 \pm 0.8mm$ determined using the physical space coordinates of the rod phantom and is better than the $2.6 \pm 1.1mm$ determined using the CT space coordinates of the rod phantom. This may due to the large error consistently produced on one of the points. In comparison the accuracy of commercial systems ranges from $1.03mm$ for the Magellan Frameless Stereotactic System (Zaaroor, et al, 2001) to $2.26 \pm 0.83mm$ for the SMN Probe (Benardete, et al, 2001). The photogrammetric system accuracy is in the right ballpark.

The repeatability of the system was determined to be $1.9 \pm 1.1mm$ with a maximum difference of $4.7mm$ between repeated measurements of the same point. Compared to systems commonly in use, this is a low repeatability. The precision or repeatability of commercial systems has been measured as $0.2mm$ for the ISG Viewing Wand and $0.36mm$ for the SMN Probe (Benardete, et al, 2001). However, the slice viewer displaying the position of the tip of the probe shows the cross on the imaged ball bearing for each measurement. The cross moves around the imaged area of the ball bearing but not off it. Positioning the tip in the same position on the ball bearing each time is difficult, so that human error is introduced into this measurement.

The accuracy of the camera calibration was determined to be $0.9 \pm 0.5mm$ with an absolute maximum error of $2.1mm$. Ideally the accuracy should be below $0.5mm$ and therefore improve the overall system accuracy, although we are satisfied with the

accuracies achieved. The accuracy could be improved by using higher resolution cameras; the current resolution of $512 \times 492 pixels$ is low compared to currently available camera resolution.

The recognition accuracy was determined to be $0.6 \pm 0.3mm$ with an absolute maximum of $1.4mm$. A measurement is rejected if the maximum error in one of the axes is above $1.2mm$ and the mean RMSE is above $0.7mm$. The software provides an option to manually select the markers, so that the surgeon has a measure of control over the system accuracy.

The registration accuracy was determined to be $0.9 \pm 0.4mm$ using four fiducials. The achieved accuracy is excellent compared with a study by Wolfsberger, et al. (2002) using the Philips EasyGuide Neuro. The RMSE of the registered volume was reported to be $2.9 \pm 1.0mm$ using adhesive skin markers similar to the fiducials used on the head phantom. However, skin movement was not a factor in the present study and is taken into account in the Wolfsberger study. The registration accuracy may therefore decrease when used on a patient where skin movement is introduced. Steinmeier, et al. (2000) found that the calculated registration accuracy does not correlate with the system accuracy.

The study by Steinmeier reported an accuracy of $1.59 \pm 0.29mm$ when using eight scattered fiducials and $3.86 \pm 2.19mm$ with four clustered fiducials. The study concludes that the attachment pattern of the markers critically influences the accuracy of the system. I did not investigate in this study the effect of different marker attachment patterns.

7.3.2 Theatre

The accuracy of the system is determined to be $1.6 \pm 0.8mm$ with an absolute maximum of $3.9mm$. This is comparable to the accuracy of $2.0 \pm 1.0mm$ determined in the

laboratory using the head phantom. However, only the fiducial markers were used to test the accuracy in theatre. The mean accuracy is comparable to the mean accuracy of $1.8 \pm 1.0mm$ determined in the laboratory using only the fiducials. The range of values obtained is narrower in theatre as is shown in the lower standard deviation. The accuracy is very good when compared to the commercial systems mentioned previously. Eliashar, et al. (2003) reported a localization error mean of $1.6mm$ and Peng (2002) reports an accuracy of $1.9 \pm 0.9mm$ using electromagnetic navigation. The system accuracies measured in theatre and in the laboratory are comparable to the reported accuracies.

The repeatability error of the system is $3.8 \pm 1.4mm$ with an absolute maximum difference between two measurements of the same point of $6.0mm$. This is very low compared to the repeatability of $1.9 \pm 1.1mm$ determined in the laboratory.

The recognition accuracy is determined to be $0.6 \pm 0.3mm$ with an absolute maximum error of $1.4mm$. This is identical to the recognition accuracy of $0.6 \pm 0.3mm$ determined in the laboratory. Although this is very good the operating lights considerably affect the recognition of the markers. The cameras pick up reflections off the surgical drapes and the handle of the probe, amongst other things. On several of the measurements the recognition error is large and the measurement is therefore rejected. The source of the errors is determined to be due to the reflection off the probe handle being seen as a marker. The reflection off the surgeon's hand often obscures the marker preventing accurate detection. The probe could be anodised black to reduce this error.

The calibration accuracy in the x- and y-axes is similar, differing by less than $0.1mm$ in the mean. The effect of the lights is more noticeable in the z-axis. The difference between the lights being directed away from the frame and turned off is negligible. The lights increased the errors in the z-axis by roughly 80% when directed at the frame. This is due to the lumen produced around the markers from the reflection of the lights. A possible solution to the problem would be to attach a shield around each marker so that only the infra-red from the cameras is reflected back. However, the decrease in

accuracy is not large enough to significantly affect the system accuracy and other solutions such as manual marker recognition are available in situations where calibration fails.

The cameras have been fitted with infra-red filters to reduce the effect of spurious reflections on the recognition of the markers.

The demonstration of the system to the Neurosurgeons involved in the project was successful. The surgeons are happy with the operation and accuracy of the system.

CHAPTER 8

Conclusions

The Prototype Navigator has very good accuracy and with an experienced professional it has been successfully used in several operations. However, the system has several notable limitations. A high level of concentration is required when positioning the reflection of the LED on the centre of three markers by sight to perform a single measurement. This process requires a finite time of about a minute and the user must be experienced in order to position the LED accurately. In addition, the equipment is bulky and difficult to transport. The mirror is positioned close to the bed in the space in which the nurses move around. If the mirror is bumped the patient needs to be re-registered using the burr holes drilled during the craniotomy.

Although the accuracy of the Zebris system is good, poor repeatability makes it unsuitable for application in neurosurgery.

In this study, stereo-photogrammetry was chosen as the most feasible alternative to the Metrograph for an interactive image-guided system. The system was developed and successfully demonstrated to the Neurosurgeons involved in the project. Good accuracies were achieved with the system both in the laboratory and in theatre. The accuracies are comparable to those reported for commercially available systems.

The disadvantage of the smart cameras is that they are very slow, although the processor is 206MHz. The marker detection routine executes very slowly on the cameras, taking approximately 10 seconds to complete and download data to the laptop. The same routine executes practically instantaneously on an 866MHz computer. At the start of the project the smart cameras presented an excellent opportunity to develop a fast, reliable navigation system, however, with current advances in technology the processing speed of computers has increased and the

relative cost decreased. Consequently, the use of a smart camera does not significantly increase the system speed. The resolution of off-the-shelf digital cameras has increased significantly and the cost decreased over the last few years making them a viable option. This could result in a significant decrease of overall system cost.

The main advantage of the smart cameras is that with the addition of an LCD display, a hard drive, mouse and/or keyboard, the system software can be modified to run on the cameras as a stand-alone system. In this case, the use of smart cameras is justified.

The accuracy of the system is comparable with systems in commercial use and has been approved by the neurosurgeons involved for use in clinical trials. Currently the system requires setting up by someone familiar with it but once in operation it is simple and easy to use. It will be modified to use off-the-shelf digital cameras or to function as a stand-alone system and developed into a commercially viable product, targeted specifically at hospitals in developing countries.

REFERENCES

Abdel-Aziz YI, Karara HM, 1971. Direct Linear Transformation from comparator coordinates into object-space coordinates in close-range photogrammetry. Proceedings on the ASP Symposium on Close Range Photogrammetry, Falls Church.

Barnett GH, et al., 1998. Surgical Navigation System Technologies in Image-guided Neurosurgery, edited by Barnett GH, et al., Quality Medical Publishing Inc., Missouri; pp 17-30.

Barnett GH, et al., 1999. Frameless stereotaxy with scalp-applied fiducial markers for brain biopsy procedures: experience in 218 cases. In J Neurosurgery 91: 569-576.

Benardete EA, et al., 2001. Comparison of Frameless Stereotactic Systems: Accuracy, Precision, and Applications. In Neurosurgery, 49(6): 1409.

Bonsanto MM, et al., 2001. Initial Experience with an Ultrasound-Integrated Single-Rack Neuronavigation System. In Acta Neurochirurgica (Wien), 143: 1127-1132.

Brown DC, 1971. Close-Range Camera Calibration. In Photogrammetric Engineering, 37(8): 855-866.

Chen HJ, 2001. Clinical experiences in neuronavigation. In Stereotactic Functional Neurosurgery, 76(3-4): 145-147.

Cooper MAR, Robson S, 1996. Theory of Close-range Photogrammetry. In Close Range Photogrammetry and Machine Vision, edited by KB Atkinson, Whittles Publishing, Caithness, Scotland; pp 26-27.

Eliashar R, et al., 2003. Image-guided navigation system – a new technology for complex endoscopic endonasal surgery. In Postgraduate Medical Journal, 79(938): 686-90.

Fryer JG, 1996. Introduction. In Close Range Photogrammetry and Machine Vision, edited by KB Atkinson, Whittles Publishing, Caithness, Scotland; pp 1-7.

Fryer, 1996. Camera Calibration. In Close Range Photogrammetry and Machine Vision, edited by KB Atkinson, Whittles Publishing, Caithness, Scotland; pp 156-175.

Fryer JG, 1989. Camera Calibration in Non-Topographic Photogrammetry. In Non-Topographic Photogrammetry, 2nd Edition, edited by HM Karara, American Society for Photogrammetry and Remote Sensing, Virginia, USA; pp 59-70.

Germano IM, et al., 1999. Clinical Use of the Optical Digitiser for Intracranial Neuronavigation. In Neurosurgery, 45(2): 261.

Gronningsaeter A, et al., 2000. SonoWand, an Ultrasound-based Neuronavigation System. In Neurosurgery, 47(6): 1373-1380.

Grunert, et al., 2003. Computer-aided navigation in neurosurgery. In Neurosurgical Rev.; 46(4): 208-14.

Gumprecht HK, et al., 1999. Brainlab VectorVision Neuronavigation System: Technology and Clinical Experience in 131 cases. In Neurosurgery, 44(1): 97.

Haase J, 1999. Neuronavigation. In Child's Nervous System, 15: 755-757.

Heilbrun MP, et al., 1993. Implementation of a Machine Vision Method for Stereotactic Localization and Guidance. In Interactive Image-Guided Neurosurgery, edited by Maciunas RJ, American Association of Neurosurgeons, USA; pp 169-177.

Karara HM, 1989. An Introduction to Non-Topographic Photogrammetry. In Non-Topographic Photogrammetry, 2nd Edition, edited by HM Karara, American Society for Photogrammetry and Remote Sensing, Virginia, USA; pp 1.

Karara HM, 1980. Non-Metric Cameras. In Developments in Close Range Photogrammetry 1, edited by KB Atkinson, Applied Science Publishers LTD, London, UK; pp 65-68.

Karara HM, Abdel-Aziz YI, 1974. Accuracy aspects of non-metric imageries. In Photogrammetric Engineering, 40(9): 1107-1117.

Kaus M, et al., 1997. Technical Accuracy of a Neuronavigation System Measured with a High-precision Mechanical Micromanipulator. In Neurosurgery, 41(6): 1431.

Kelly PJ, 2000. Stereotactic Surgery: What is Past is Prologue. In Neurosurgery, 46(1): 16.

Kim HS, Kim JH. Circle Detection Method using the Intersecting Chords. http://vivaldi.kaist.ac.kr/~iclab

Maciunas RJ, 1993. Yesterday's Tomorrow: The Clinical Relevance of Interactive Image-Guided Surgery. In Interactive Image-Guided Neurosurgery, edited by RJ Maciunas, American Association of Neurological Surgeons, USA, pp 7

McInerney J and Roberts DW, 2000. Frameless Stereotaxy of the Brain. In The Mount Sinai Journal of Medicine, 67 (4): 300-310.

Mikhail EM, et al., 2001. Mathematical Concepts in Photogrammetry. In Introduction to Modern Photogrammetry, John Wiley & Sons, Inc, New York, USA; Pg 80-106.

Mikhail EM, et al., 2001. Resection, Intersection and Triangulation. In Introduction to Modern Photogrammetry, John Wiley & Sons, Inc, New York, USA; Pg 107-126.

Peng YP, et al., 2002. Application of electromagnetic navigation in surgical treatment of intracranial tumours: analysis of 12 cases. In Di Yi Jun Yi Da Xue Xue Bao, 22(7): 662.

Raabe A, et al., 2002. Laser Surface Scanning for Patient Registration in Intracranial Image-guided Surgery. In Neurosurgery, 50(4): 797-801.

Roberts, et al., 1986. A frameless stereotaxic integration of computerized tomographic imaging and the operating microscope. In J Neurosurgery, 65: 545-549.

Roberts DW, et al., 1992. Computer Image Display during Frameless Stereotactic Surgery. In Computers in Stereotactic Neurosurgery, edited by PJ Kelly and BA Kall, Blackwell Scientific Publications, Boston, USA; pp 313-319.

Scott PJ, 1981. The Reflex Plotters: Measurement without Photographs. In Photogrammetric Record, 10(58): 435-446.

Spetzger U, et al., 2002. Error Analysis in Cranial Neuronavigation. In Minimally Invasive Neurosurgery, 45:6-10.

Steinmeier, et al., 2000. Factors influencing the application accuracy of neuronavigation systems. In Stereotactic Functional Neurosurgery; 75(4): 188-202.

Suess O, et al., 2001. Intracranial Image-Guided Neurosurgery: Experience with a new Electromagnetic Navigation System. In Acta Neurochirurgica (Wien), 143: 927-934.

Tirakotai W, et al., 2003. Image-Guided Transsylvian, Transinsular Approach for Insular Cavernous Angiomas. In Neurosurgery 53(6): 1299-1305.

Thompson, EH, 1969. An Introduction to the Algebra of Matrices with some Applications. Adam Hilger, London.

Van Geems B, 1997. The Development of a Simple Stereotactic Device for Neurosurgical Applications, PhD dissertation, University of Cape Town; pp 131-140.

Watanabe E, 1993. The Neuronavigator: A Potentiometer-Based Localizing Arm System. In Interactive Image-Guided Neurosurgery, edited by RJ Maciunas, American Association of Neurological Surgeons, USA; pp 135-147.

Watanabe E, et al., 1987. Three-dimensional digitizer (neuronavigator): new equipment for CT-guided stereotaxic surgery. In Surgical Neurology, 27: 543-547.

Wolfsberger S, et al., 2002. Anatomical landmarks for image registration in frameless Stereotactic neuronavigation. In Neurosurgical Rev., 25(1-2): 68-72.

Woydt M, et al., 2001. Ultrasound-guided neuronavigation of deep-seated cavernous haemangiomas: clinical results and navigation techniques. In British Journal of Neurosurgery, 15(6): 485-495.

Zaaroor M, et al., 2001. Novel Magnetic Technology for Intraoperative Intracranial Frameless Navigation: In vivo and in vitro results. In Neurosurgery, 48(5): 1100.

APPENDIX A

Electronic Development House (EDH) Dacst Smart Camera Specifications

The smart camera is a stand-alone digital camera equipped with a powerful StrongArm processor and area imager for intensive image processing. The smart camera is capable of being used in various applications such as image-guided surgery, machine vision, sport and mining.

The smart camera runs a version of Debian Linux adapted for the StrongArm processor board. Separate drivers, listed below, enable the client to communicate to the server and daughter board.

- Cs9800.o (network driver)
- Area-sensor.o (interface to daughter card with area-sensor hardware)
- Video-dev.o (V4L2 driver adapted for EDH)
- Init.sh (initialise network driver)
- Load.sh (load drivers)
- Uload.sh (unload drivers)
- Client (main application running on the camera)

The components of the smart camera system include a computer running Window 2000/NT, acting as the server; the smart camera, the client connected to the server; and a second computer running Linux.

The server is connected to the client via an Ethernet connection. Commands are transmitted to the smart camera from the server. The camera executes the command by either adjusting a parameter or capturing an image.

The second computer connects to the client via a serial cable. Any feedback from the client, such as debug information, will be displayed on the terminal. A separate computer is not required for a terminal since the server can be used to run software such as Hyper Terminal. However, if the main application running on the client needs to be recompiled then a computer running Linux is required.

A.1 Electrical Interface Specification

Power and IO:

- $24V$ DC nominal at $1A$
- 4 opto-isolated inputs that can be used for triggering
- 4 outputs (open collector)

Ethernet: 10Mbits/s
USB host & slave: not yet supported

A.2 Processor Specifications

Processor:

- StrongARM SA1110
- 235 Drystone $2.1MIPS$ / $206MHz$
- $1.75V$ Processor and $3.3V$ I/O
- $32bit$

Software:

- Linux real time Operating System (OS) support – $100\mu s$ maximum response time
- Complete driver support
- C-library calls for all interfaces

Interfaces:

- Camera Link (http://www.pulnix.com/CameraLink/CL-prods.html) connection to imager
- IDE connector for hard disk
- LCD ($640 \times 480 \times 256$ colours)
- $RS232$ serial port

Other:

- SDRAM: $64MB$
- FLASH: $32MB$
- Watchdog
- EEPROM
- Real time clock (battery backed up)
- PCMCIA (not yet implemented)

A.3 Area Imager Specifications

- Sony CCD
- $512 \times 492 pixel$ resolution
- Monochrome: 256 level grayscale image
- $60Hz$ frame rate

APPENDIX B

Mathematics

B.1 The Direct Linear Transformation

The direct linear transformation (DLT) as first proposed by Abdel-Aziz and Karara (1971) is a mapping from image space to object space. It transforms the 2D coordinates of a point visible on each of a number of images into the 3D coordinates of that point in real or object space.

A minimum of 6 control points are required to solve the twelve transformation parameters required for the mapping. The control frame, described in section 5.3, comprising 12 control points or markers of which the 3D coordinates are accurately known is used for this purpose. The 12 parameters of the DLT are solved using a least squares adjustment.

The DLT is defined by:

$$u_k + u_k K_k r_k^2 = \frac{L_{1k}X + L_{2k}Y + L_{3k}Z + L_{4k}}{L_{9k}X + L_{10k}Y + L_{11k}Z + 1}\ , \tag{1}$$

and

$$v_k + v_k K_k r_k^2 = \frac{L_{5k}X + L_{6k}Y + L_{7k}Z + L_{8k}}{L_{9k}X + L_{10k}Y + L_{11k}Z + 1}\ , \tag{2}$$

where:

k = L or R denotes values pertaining to the left or right images, respectively,

u_k and v_k are the x- and y-coordinates, respectively, of a point in the image,

X, Y and Z are the 3D coordinates of the point in object space,

L_1 to L_{11} denote the eleven transformation parameters,

K_k is a term that was introduced to correct for lens distortion (Karara and Abdel-Aziz, 1974) and $r_k^2 = (u_k^2 + v_k^2)$.

The parameters can be computed using a linear least squares solution. Then

$$L_k = (P_k^T * P_k)^{-1} * (P_k^T * A_k) \tag{3}$$

in which

$$L_k = \begin{bmatrix} L_{k1} \\ L_{k2} \\ \vdots \\ L_{k11} \\ K_k \end{bmatrix}, \quad A_k = \begin{bmatrix} u_{k1} \\ v_{k1} \\ u_{k2} \\ v_{k2} \\ \vdots \\ u_{kn} \\ v_{kn} \end{bmatrix} \text{ and}$$

$$P_k = \begin{bmatrix} X_1 & Y_1 & Z_1 & 1 & 0 & 0 & 0 & 0 & -u_{k1}X_1 & -u_{k1}Y_1 & -u_{k1}Z_1 & -u_{k1}r_{k1}^2 \\ 0 & 0 & 0 & 0 & X_1 & Y_1 & Z_1 & 1 & -v_{k1}X_1 & -v_{k1}Y_1 & -v_{k1}Z_1 & -v_{k1}r_{k1}^2 \\ \vdots & \vdots & & & & & & & & & & \vdots \\ X_n & Y_n & Z_n & 1 & 0 & 0 & 0 & 0 & -u_{kn}X_n & -u_{kn}Y_n & -u_{kn}Z_n & -u_{kn}r_{kn}^2 \\ 0 & 0 & 0 & 0 & X_n & Y_n & Z_n & 1 & -v_{kn}X_n & -v_{kn}Y_n & -v_{kn}Z_n & -v_{kn}r_{kn}^2 \end{bmatrix} \tag{4}$$

The subscript n denotes the number of the control point.

The DLT is solved for each camera yielding two sets of transformation parameters mapping image space to object space (i.e. 12 left parameters and 12 right parameters). The 3D coordinates (X, Y, Z) of any point visible in both the left and the right image, with image coordinates (x_l, y_l) and (x_r, y_r), respectively, can then be computed using:

$$N = (J^T * J)^{-1} * (J^T * M) \tag{5}$$

where:

$$N = \begin{bmatrix} X \\ Y \\ Z \end{bmatrix}, \quad M = \begin{bmatrix} u_l - L_{l4} + u_l * r_l^2 * K_l \\ v_l - L_{l8} + v_l * r_l^2 * K_l \\ u_r - L_{r4} + u_r * r_r^2 * K_r \\ v_r - L_{r8} + v_r * r_r^2 * K_r \end{bmatrix} \text{ and}$$

$$J = \begin{bmatrix} L_{l1} - L_l 9 * u_l & L_{l2} - L_{l10} * u_l & L_{l3} - L_{l11} * u_l \\ L_{l5} - L_l 9 * v_l & L_{l6} - L_{l10} * v_l & L_{l7} - L_{l11} * v_l \\ L_{r1} - L_r 9 * u_r & L_{r2} - L_{r10} * u_r & L_{r3} - L_{r11} * u_r \\ L_{r5} - L_r 9 * v_r & L_{r6} - L_{r10} * v_r & L_{r7} - L_{r11} * v_r \end{bmatrix} \tag{6}$$

in which l and r denote values pertaining to the left or right images, respectively.

B.2 The Rodrigues Transformation

The Rodrigues Transformation (Thompson, 1969) is used to transform coordinates from one 3D system to another where both systems have a common origin. The following equation is used:

$$\begin{bmatrix} u \\ v \\ w \end{bmatrix} = R^T * \begin{bmatrix} x \\ y \\ z \end{bmatrix} \tag{7}$$

where:

u, v, w are the 3D coordinates of a point in one system and

x, y, z are the 3D coordinates of the point in the second system

then

$$R = \frac{1}{\Delta}\begin{bmatrix} 1+\frac{1}{4}*(\lambda^2-\mu^2-\upsilon^2) & -\upsilon+\frac{1}{2}*\lambda*\mu & \mu+\frac{1}{2}*\lambda*\upsilon \\ \upsilon+\frac{1}{2}*\mu*\lambda & 1+\frac{1}{4}*(-\lambda^2+\mu^2-\upsilon^2) & -\lambda+\frac{1}{2}*\mu*\upsilon \\ -\mu+\frac{1}{2}*\upsilon*\lambda & \lambda+\frac{1}{2}*\upsilon*\mu & 1+\frac{1}{4}*(-\lambda^2-\mu^2+\upsilon^2) \end{bmatrix} \quad (8)$$

with

$$\Delta = 1+\frac{1}{4}*(\lambda^2+\mu^2+\upsilon^2) \quad (9)$$

In (8) λ, μ and υ are known as the Rodrigues parameters. They describe three rotations around the coordinate axes, a scale transformation and a translation of the origin. A minimum of three points common to both systems are required to solve for the parameters.

APPENDIX C

SIIGNS Manual

C.1 Procedure

1. CT scanning of lesion and fiducials
2. Download CT images to the laptop
3. Digitisation of CT images
4. Theatre set-up
5. Camera calibration
6. Patient registration
7. Craniotomy and burr points
8. Surgery
9. Recalibration of cameras and patient re-fix

C.1.1. CT scanning of lesion and fiducials

- Position the (± 4) fiducial markers on the scalp around the lesion
- Scan the lesion
- Number the fiducials
- Scan the fiducials in order
- Move the images to the Groote Schuur Hospital (GSH) network or copy to CD

C.1.2. Download CT images to the laptop

For GSH Picker Scanner:

- Connect laptop to the GSH network
- Log in to server:
  - Server: **Curie**
  - Supply password to connect to \\TPP-797\IMAGES (J:)
- Go to **J:** drive (Images on **TPP-797**)
- Copy image files to image directory on laptop usually **C:\Siigns\Patient**

Otherwise

- Copy images from CT to **C:\Siigns\Patient** directory on laptop

C.1.3. Digitisation of CT images

- Boot up laptop
- Load SIIGNS interface software
  - Click *Patient Details*
    - Click *Name*
      - Enter the first 4 letters of the patient's name
      - Select CT scanner type: LHS or RHS
  - Click *Digitise*
    - Click *Open CT Images*
      - Opens MRIPointWin
      - Click *File*
        - ❖ **Click *Open Dicom file***
          - Load the CT images in c:\Siigns\Patient
          - Click *Add ROI*
            - ➢ Outline tumour regions
            - ➢ Proceed to next image
          - Click *Add Marker*
            - ➢ Click on fiducial markers
            - ➢ Proceed to next image

- Click *Save ROI and Marker Info*
- Set threshold to 350
- Click *Save 3D File*

- Close MRIPointWin

- Click *Open 3D Viewer*
  - Click *File*
    - ❖ Click *Open*
      - Load 3D image header file (***.h3r**)

C.1.4. Theatre Set-up

- Clamp the stand to the rails on either side of the surgical bed
- Attach camera enclosure to tripod mount on the stand
- Connect to laptop via an Ethernet connection
- Boot up cameras
- Load client software on camera using FTP and telnet
  - Open from *Start* Menu: **WS_FTP95 LE**
    - Open session for ArmCam1
      - Transfer **ClientL** from **C:\Siigns** to **\tmp** directory on the camera
    - Close Session
    - Open Session for ArmCam2
      - Transfer **ClientR** from **C:\Siigns** to **\tmp** directory on the camera
    - Close Session
    - Exit WS_FTP95 LE

  - Telnet from MS-Dos onto each camera using their IP addresses
    - ArmCam1: **telnet 137.158.18.3**

        - Type **cd tmp** press **Enter**
        - Type **chmod 777 clientl** press **Enter**
        - Type **./clientl –ip 137.158.18.5** press **Enter**
    - ArmCam2: **telnet 137.158.18.4**
        - Type **cd tmp** press **Enter**
        - Type **chmod 777 clientr** press **Enter**
        - Type **./clientr –ip 137.158.18.5** press **Enter**
    - Minimise telnet windows

C.1.5. Camera Calibration

- Click *Calibrate Cameras*
    - Click *Focus Cameras*
        - Focus cameras on the area at the head of the bed
        - Hold control frame in place above the head of the patient
        - Ensure that the entire frame and all markers are visible in the field of view of each camera
    - Click *Calibrate Cameras*
        - Calibrates cameras and displays the accuracy of the calibration
        - Remove control frame

C.1.6. Patient Registration

- Click *Patient Fix*
    - Position the probe with its tip on the first fiducial marker
    - Click *OK*
    - Repeat for all fiducial markers in the same order as scanned
    - The accuracy of registration is displayed

- Click *Verify Entry Area*
    - Enter the 3 best fiducial markers to be used as burr points
    - Click *OK*
        - Measures the position of the tip of the probe
        - Displays the tip position on the nearest CT slice
        - Use to check the accuracy of the Patient Registration and to check for critical structures along the proposed trajectory

C.1.7. Craniotomy and Burr Points

- The surgeon performs the craniotomy and drills 3 burr points
- Click *Burr Points*
    - Position the probe with its tip on the first burr point
    - Measure all 3 in order

C.1.8. Surgery

- The surgery is performed
- To measure:
    - Place tip of probe in position
    - Click *Tip and Stereo*
        - Computes the tip position
        - Displays the position on the 3D image and the nearest CT slice

C.1.9. Recalibration of Cameras and Patient Re-fix

- If the cameras are moved
    - Recalibrate following same procedure as earlier

- Perform Patient Refix

- If patient is moved
  - Click *Patient Refix*
    - Enter the first four letters of the patients name
    - Position the tip of the probe on the first Burr Point
    - Measure all 3 in the same order as before
    - The accuracy of the re-registration is displayed